

SUPERCRITICAL FLUID FLOW IN PIPELINES - A DENSE PHASE CASE STUDY

Hamed Ghasvari-Jahromi ^{a1}, Fatemeh Ekram ^a, Chuntao Deng ^b, Jim Knudson ^b, Satya Mokamati ^a

^a Vanmok Leak Detection Technologies

^b Keyera Corporation

© Copyright 2022, PSIG, Inc.

This paper was prepared for presentation at the PSIG Annual Meeting held in San Antonio, Texas, 16 May – 19 May 2023.

This paper was selected for presentation by the PSIG Board of Directors following review of information contained in an abstract submitted by the author(s). The material, as presented, does not necessarily reflect any position of the Pipeline Simulation Interest Group, its officers, or members. Papers presented at PSIG meetings are subject to publication review by Editorial Committees of the Pipeline Simulation Interest Group. Electronic reproduction, distribution, or storage of any part of this paper for commercial purposes without the written consent of PSIG is prohibited. Permission to reproduce in print is restricted to an abstract of not more than 300 words; illustrations may not be copied. The abstract must contain conspicuous acknowledgment of where and by whom the paper was presented. Write Librarian, Pipeline Simulation Interest Group, 945 McKinney, Suite #106, Houston, TX 77002, USA – info@psig.org.

ABSTRACT

There is a discontinuity in the tabulated thermodynamic properties as the fluid is going across the critical point. In this paper, utilizing regularization techniques, correlations are established to continuously determine fluid properties during the transition through the critical point and into the supercritical region.

An augmented model for the dense phase is proposed by integrating our derived correlations into the conservation equations. The implementation of the augmented model is presented for a pipe network carrying ethane. The performance improvements that the proposed correlations when used in the augmented model can offer to CPM-based leak detection algorithms are discussed in detail.

A novel equation describing the limit behavior of the adiabatic heat index at the supercritical point is introduced, resulting in an updated correlation for maximum flow rate at choked conditions. The values from a certain hole size are obtained theoretically from the presented equations for a case study of NGL and condensate transmission pipeline rupture incident.

An attempt is made to improve the sensitivity of leak detection systems, which is the minimum detectable hole sizes, with and without the regularized correlations presented in this paper. The minimum theoretical sizes of detection for a given model are estimated.

INTRODUCTION AND BACKGROUND

Transportation of natural gas and CO₂ in their dense phase through pipelines is getting more attention due to the beneficiary aspects of it. Dense phase fluid has a higher density than gas and lower viscosity than liquid and reduces both the required pipe diameter and the pressure drop along the pipe.

The real-time transient modeling (RTTM) of the transmission pipelines with the compressible flow is challenging due to the varying properties of the fluid itself. Even with precise measurements of flow, pressure, and temperature, the accuracy of the model depends on the precise calculation of the fluid properties. In this paper, the effectiveness of the compressibility factors and generalized compressibility chart in density calculations were assessed, and the standard and modified equations of states were compared. However, as the fluid passes the critical point the uncertainties in the calculated density from these methods increase.

The results from the augmented model are presented for a pipe network carrying ethane, including two 35 Km (21.75 miles) branches, 4 and 6 inches (101.6 mm and 152.4 mm) in diameter, both pipe sections are buried and non-insulated. A separate section addressing leak detection in pipelines carrying dense-phase supercritical fluids is included before the conclusion. Real-time density calculations under degraded conditions associated with the supercritical state help prevent false alarms and increase the reliability and robustness of the leak detection system.

We demonstrate that it is possible to quantify the improvement in sensitivity of leak detection systems for dense fluids using CPM-based models that employ appropriate models for simulating these fluids and their transient conditions in a pipeline. The minimum detectable hole sizes using the regularized correlations presented in this paper are shown for the shut-in condition, for which determining the intensity of the leak in terms of percentage relative to the hole size is not meaningful.

¹ Corresponding author: hamed@vanmok.com

APPROACH AND ANALYSIS

THERMOFLUID MECHANICAL ASPECT OF THE PROBLEM

Dense Phase Fluid Properties

The fluid is considered a dense phase when its temperature and pressure are above its critical point. Dense phase fluids, often found in the petroleum and natural gas industries, are characterized by their high density, low viscosity, and low surface tension. When these fluids approach their supercritical point, the thermodynamic properties change dramatically, leading to a significant impact on the hydrodynamics and heat transfer behavior in pipelines. This can result in non-linear and non-ideal flow conditions, making the accurate prediction of real-time pipeline states a challenging task [1].

The critical point of ethane is 32.17 °C and 4.87 MPa. Figure 1 shows the ethane phase diagram and the pipeline operating zone. The operating pressure of the ethane pipeline is well above its critical pressure and depending on the temperature of the fluid the ethane transfers either as a compressible liquid or a supercritical fluid. Figure 3 represents the T-S diagram for ethane.

The fluid properties of the Ethane pipeline depend on the composition, temperature, and pressure. Therefore, the properties are calculated based on the values of pressure and temperature transmitters. The more frequent the transmitters' values, the more precise will be the properties.

It is usual to use the compressibility factor (Z), predicted by a proper equation of state to calculate the fluid density using Equation ($\rho=P/ZRT$).

The compressibility factor is a measure of the deviation from the ideal gas behavior. Traditionally, the compressibility factor is defined for gases but is commonly used for liquids as well. Figure 2 shows the compressibility factor vs pressure at different temperatures for Ethane. The values of the compressibility factor for the liquid phase are small and far from unity as expected.

The compressibility factor is known to be the same for any pure gas at the same reduced temperature (T_r) and reduced pressure (P_r).

Hence, the pressure and temperature were represented in their reduced forms in Figure 2 similar to the generalized charts for the compressibility factor. The compressibility factor emerged as a crucial parameter influencing the flow behavior of supercritical fluids. Figure 27, Figure 28 and Figure 29 display the compressibility factor for temperatures below (20 C), above (40 C) and equals to critical temperature, respectively.

The equations of state are used to calculate the thermodynamic properties of a matter such as density. The most recent equations of state are formulated using a form of Helmholtz free energy, first proposed in 1985 by Schmidt and Wagner.

Accurate density calculations from the Schmidt and Wagner equation of state (SWEOS) are possible when the fluid is far enough from the critical condition. Uncertainties in calculations of the liquid ethane density, between 27°C and 32°C and below 10 MPa are estimated to be 0.5%. However, as the fluid passes the critical point and the temperature goes above the critical temperature of 32.17°C and the pressure surpasses the critical pressure of 4.87 MPa, the uncertainties in the calculated density can be more than 5% [2].

After the effectiveness of the compressibility factors and generalized compressibility chart were assessed, and the standard and modified equations of states were compared, it is confirmed that the best approach for the dense phase fluid in the pipeline under the study is the correctional correlations, which are derived from thermal properties of matter and shaped into thermodynamics functional. This functional becomes an auxiliary equation like a constitutive equation. This auxiliary constitutive equation is coupled with the appropriate model to simulate the transient and compressible flow.

Singularity of Supercritical Region

Regularization methods employed in this research are utilized to determine analytical functions relating properties to their reduced counterparts, such as the relationship between reduced density and pressure or reduced density and temperature. These are not limited to ethane or methane but also can similarly cover propane, butane, and CO₂.

This suggests that these functional forms may also capture a type of physics between those properties near the vicinity of the supercritical point. The correlations and the conservation equations of mass, momentum, and energy form an augmented model for the dense phase transportation in pipelines.

Correlations employing regularization techniques near the discontinuous regions of substance properties are presented. These correlations facilitate the calculation of properties at critical pressure as a function of reduced temperature, and at critical temperature as a function of reduced pressure.

Equations (I) and (II) represent the correlations for reduced density and heat capacity ratio of ethane, respectively. The parameters for these equations can be found in Table 3 and Table 4.

$$\rho_r = a + bx + \frac{c}{1 + de^{-k(x-1)}} \quad (I)$$

Table 1- Parameters for the density correlation

x	y	R ²	a	b	c	d	k
T _r	ρ _r	1	5.313	-4.666	0.883	2.992	-544.14
P _r	ρ _r	1	-2.042	2.734	0.571	1.034	522.83

Figure 10 and Figure 11 show the reduced density vs T_r and P_r, respectively. The heat capacity correlation for T_r and P_r as independent variables are presented in Figure 12 and Figure 13.

$$\gamma = b + \left| \frac{a}{x-1} \right|^c \quad (\text{II})$$

Table 2- parameters for the heat capacity ratio correlation

x	y	R ²	γ-max	a	b	c
T _r	γ	0.99	17.78	0.037	1.483	0.773
P _r	γ	0.99	52.15	0.352	1.014	0.671

The variation in the properties of methane, ethane and CO₂ has been shown in Figure 14 to Figure 24 at different temperature and pressures.

When instead of the values of parameters at the nodes, we have the functions on the edges, transfinite interpolation applies (see Appendix 2).

AUGMENTED MODEL

Governing equations, Numerical Aspects

Beginning with the three conservation laws—continuity, momentum, and energy- the numerical solution for hyperbolic PDEs can be obtained using the method of characteristics (MOC) (details are available in [8]).

The key difference for semi-compressible fluids, such as during column separation or cavitation (also known as slack conditions), is that the governing equations are A1.33 and A1.34. Equation A1.7 demonstrates the longitudinal energy balance and can be used in conjunction with A1.33 and A1.34.

However, for compressible fluids or dense phase conditions, significant density changes result from heat transfer and temperature fluctuations, causing the governing equations to become highly nonlinear and coupled compared to the semi-compressible fluid equations. These equations take the form of A1.1 to A1.7, expressed in terms of enthalpy and internal energy, as seen in equation A1.3.

The first three equations (A1.1 to A1.3) represent the initial forms of the continuity, momentum, and energy equations,

respectively. The subsequent three equations are restructured in terms of the pipeline's independent variables (Pressure(P), flow rate(q) and temperature(T)).

Given the nonlinear nature of the governing equations for the model PDE and the authors' experience working with numerical simulations of hyperbolic type PDEs, it was determined that the smoothness of results as a function of temperature could be better achieved using the Method of Lines (MOL). This approach provides the numerical solution for the documented mathematical model when combined with the derived correlations over a range of supercritical conditions, utilizing an analytical function to facilitate numerical calculations.

Heat Transfer Consideration

In the implementation of the energy equation to the model, the composite structure of a typical hydrocarbon transmission pipeline is considered. As shown in Figure 4 and Figure 5, there are thermal layers including the wall thickness, the insulation thickness, and the skin of the pipe and the ground for a buried pipeline). Together, these layers provide a net effect for the lateral heat transfer as the overall heat transfer coefficient and are usually denoted by U_∞. The overall heat transfer coefficient was found to be a crucial parameter that affects the temperature distribution along the pipeline.

An analogy exists between the diffusion of heat and electrical charge. Similarly, to how electrical resistance is associated with the conduction of electricity, a thermal resistance can be associated with the conduction of heat. Resistance is defined as the ratio of a driving potential to the corresponding transfer rate. This concept is illustrated in Figure 6, where thermal resistances form a complete circuit.

Composite walls can also be characterized by parallel-series configurations, as shown in Figure 6. Although heat flow is multidimensional, it is often reasonable to assume one-dimensional conditions. Under this assumption, different thermal circuits result in four distinct nodes. For instance, interior nodes will not experience radiation, as they are buried. However, the beginning and end nodes may be exposed, resulting in substantial differences in the total heat transfer coefficient associated with these control volumes. This is particularly relevant during seasons with extreme temperatures or due to general changes in radiation flux on these exposed portions.

The thermal layers, comprising the ground, pipe skin, and wall, were discovered to substantially impact the overall heat transfer coefficient. Figure 6 displays all the thermal resistances involved in heat transfer from the fluid inside the pipe to the surroundings, assuming the pipeline is not insulated. The equivalent resistance for heat transfer is provided in Equation A1.19, while R_G is calculated using Equation A1.20. R₁, R₂, and R₃ represent parallel resistances. R_G and R_{rad} are also parallel and in series with R_w. In Equation A1.19, the two sets of

resistances within parentheses are also parallel to each other as reflected in Equation A1.19 using “||”.

The resistance of the ground was assumed to be constant, however there is an error associated with this assumption. The right-hand side of Equation A1.21 shows the error associated with the constant assumption of the temperature of the ground. Erf is the gaussian error function for which numerical values are available. The error will be less than 1% if the burial depth is 3 meters even if the period of the consideration is beyond 7 to 8 days, however at the depth of 1.5 meter, which this pipeline is buried the error does not exceed 5% up to 29 days.

Although calculating τ_t (Equation A1.35)- for the fluid of each control volume and the cylindrical shell encapsulating it as separate boundaries- provides significant insights into the physics of the problem, determining the Biot number is usually the first step to assess whether the Lumped Capacitance Method (LCM), which simplifies the approach by neglecting the spatial effects of heat transfer, is appropriate or not.

The criterion for using LCM is a Biot number (Bi) of 0.1 or less. In our case, except for specific conditions, a Biot number less than 0.1 is never guaranteed. Consequently, the gradients within the mediums cannot be neglected and must be addressed.

INITIAL AND BOUNDARY CONDITIONS, PIPELINE CONFIGURATION

Liquid ethane flows through the pipe, and its pressure, volumetric flow rate, and temperature are recorded right before it separates into two branches, each 35 Km long with a diameter of 6 inches (152.4 mm) and 4 inches (101.6 mm). These two branches are rejoined at the end of 35 Km and the pressure transmitter, flowmeter, and thermometer are available to record their state at the delivery. The characteristics of the pipeline are summarized in Table 3.

The main components of the pipeline throughput along with their properties at the critical point are presented in Table 4. Figure 7 shows the elevation profile of the pipeline which is identical for both branches.

Table 3- Pipeline characteristics

Pipe outer diameter	101.6 mm (4 in) and 152.4 mm (6 in)
Pipe wall thickness	4.8 mm (0.19 inches)
Pipeline length	35 km (21.75 miles)
Pipe roughness	50 μm (0.002 inches)
Pipe burial depth	1.5 m (5 ft)

The monthly average of the operating pressure and temperature of the line was presented in

Figure 8 starting from October 2020 to June 2021. In late June 2021, a historic record was set for Alberta as the warmest June

on record. This extremely hot temperature gives us a spectacular opportunity to observe the effects of global warming on the ethane pipeline and study the behavior of dense phase flow (see Figure 9).

The heat loss along the pipeline decreased as the ambient temperature increased, increasing the flowing fluid temperature.

1. Temperature: The average high temperature in Edmonton during June is around 21°C (70°F), while the average low temperature is around 8°C (46°F). However, temperatures can vary widely depending on the time of day and other weather factors.
2. Precipitation: June is typically one of the wetter months in Edmonton, with an average of 70 mm (2.8 in) of rainfall. This can have an impact on pipeline conditions, as water can cause corrosion and other damage over time.
3. Atmospheric Pressure: The average atmospheric pressure in Edmonton during June is around 100.9 kPa (29.8 inHg). However, this can also vary depending on weather conditions, such as storms or high winds.

Overall, these weather properties can give insight into how Edmonton's climate can affect pipelines and other infrastructure in the region. It's important to consider these factors when analyzing data from pipelines to better understand their performance and any potential maintenance needs.

Table 4- Critical properties of the main components of the pipeline's throughput

Component Mole fraction%	T_{cr}	P_{cr}	D_{cr}
CO ₂	304.1 K	7.38 MPa	467.6 Kg/m ³
3%	87.7 F	1070.4 Psi	29.2 lb _m /ft ³
CH ₄	190.6 K	4.6 MPa	162.2 Kg/m ³
2%	-116.6 F	667.2 Psi	10.1 lb _m /ft ³
C ₂ H ₆	305.3 K	4.87 MPa	206.2 Kg/m ³
95%	89.9 F	706.3 Psi	12.9 lb _m /ft ³

DENSE PHASE LAEK ASPECTS

The simulation of dense phase fluids in pipelines, particularly near the supercritical point, is crucial for understanding and optimizing the flow and heat transfer behavior of these fluids.

This knowledge is indispensable for designing reliable and robust leak detection algorithms that can perform effectively across various degraded operating conditions, such as during the supercritical thermodynamical state of dense phase fluids like CO₂, ethane, or mixtures of natural gas liquids.

These fluids often experience complex flow and heat transfer phenomena due to their proximity to the supercritical point, which is the critical point where the distinction between liquid

and gas phases disappears.

A better understanding of dense-phase fluids transportation in pipelines and accurate mathematical models of these phenomena are essential for designing effective leak detection algorithms, ensuring the safety and efficiency of pipeline operations, and minimizing environmental impacts.

Leak detection in transmission pipelines carrying dense phases is challenging due to the varying properties of the fluid itself.

Even with precise measurements of flow, pressure, and temperature, the performance of a leak detection system depends on the accurate calculation of the fluid. Pipelines carrying dense phase fluids can experience various degraded operating conditions, such as pressure fluctuations, temperature changes, and flow regime transitions.

These conditions can cause the fluid to enter a supercritical thermodynamic state, further complicating the hydrodynamic and heat transfer behavior. This paper evaluated the practical aspects of supercriticality in a dense phase transmission pipeline.

The accurate prediction of real-time pipeline states is critical for designing and implementing leak detection algorithms. As dense phase fluids near the supercritical point can exhibit unpredictable behavior, leak detection algorithms need to be robust and adaptable to different operating conditions.

By incorporating advanced mathematical models of fluid flow and heat transfer, these algorithms can continuously monitor the pipeline's performance, identify potential leaks, and initiate appropriate corrective actions.

RESULTS

TEST CASES

The objective is to build confidence in the solutions for pressure, temperature, velocity, and density fields, along with all associated thermal and physical properties. We want to determine whether this model can predict other phenomena related to supercritical dense phase fluid flow. This encompasses line packing, a prevalent practice in fluid transportation studies.

Additionally, the research explores the simulation of novel physical phenomena, like the fluid at rest inside the pipe, which poses challenges even for incompressible fluids.

Finally, we assess the model's potential for leak detection and consider a range of scenarios that could emerge in dense phase fluid transportation.

The Method of Lines (MOL) is employed to approximate the governing Partial Differential Equations (PDEs), and the resulting Ordinary Differential Equations (ODEs) are solved

numerically to acquire a numerical solution.

Prior to testing the model, initial conditions must be determined according to the pipeline configuration and instrumentation. Experimental validation of the model's predictions, however, is challenging due to the highly nonlinear nature of the problem and the absence of general analytical solutions. Also, laboratory tests cannot simulate the rather complex situations as occur in an industrial scale pipeline considering its specific elevation profile and aspect ratio ($L/D \gg 1$).

Consequently, benchmark problems must be utilized to verify the predictions. The model is an augmented comprehensive model, which can be used for dense phase fluids as well as semi-compressible and incompressible fluids.

Benchmark problems typically involve the modeling of compression waves and transient conditions such as valve closures or line packing.

DISCUSSIONS OF REALISTIC CASES

The line packing observed in the pipeline under the study is investigated. Additionally, the occurrence of kink-like behavior in pipelines during shut-in period is analyzed, which is caused by differing heat transfer rates in the morning and afternoon of hot days when surrounding temperatures approach or surpass the substance's supercritical temperature.

Line Packing

The impact of line pack pressures on short pipes is negligible, but they must be considered for longer pipe systems, regardless of density fluctuations. For incompressible fluids, the line pack pressure is comparable to water hammer pressures and surpasses them in transmission lines exceeding 15 km (10 miles).

In an isothermal line packing, density increases proportionally to the increase in pressure due to valve closure or another similar throttling process. Hence, for the same amount of mass flux less value metric flow rate will occur.

This can temporarily cause a negative mass balance resulting in the issue of a possible false alarm. The resolution of this matter is an interesting, applied problem with interesting physical features and a unique methodology of approach.

As illustrated in Figure 26, the line pack pressure increases significantly more than Joukowsky criteria when dealing with dense phase fluids. This increase can be up to five times greater than Joukowsky's criteria within approximately two reflection times. Each reflection time is defined as twice the pipe length divided by the speed of sound.

By utilizing these time and pressure characteristics, the line pack plot in Figure 26 validates the augmented model's

effectiveness and the accuracy of the numerical predictions generated by its solution. This model adeptly addresses the physical phenomena associated with dense phase compressible fluids such as CO₂ and NGL.

Kink-like Behavior during Shut-in

The shut-in condition provided for the pipeline (Figure 31) offers an excellent opportunity for reliable algorithm initialization, as the temperature is fairly uniform during certain times of the day. Since the physics of the problem involve a marching-in-time nature, proper initialization is crucial for synchronizing the real-time transient model predictions with the actual pipeline behavior. If the appropriate initialization and model are employed, the model should be capable of predicting the real-time behavior of the dense phase fluid inside the pipeline under various operating conditions, ranging from running to shut-in states, and accounting for temperature fluctuations during shut-in periods.

This creates an accurate digital twin, enabling simulated leak tests or other pipeline examinations to be conducted in a simulation environment while maintaining synchronization and precise matching with the real-time state of the pipeline. This accuracy is contingent on the continuous reception of the required boundary conditions, ensuring that the digital twin model predictions remain reliable.

Figure 30 and Figure 31 illustrate the authentic transient behavior of the ethane pipeline during an extended shut-in condition. The analysis of this period, along with the exploration of previously unaddressed phenomena observed in these long-range temporal boundary conditions, is the focus of this section.

Over the 24-hour shut-in simulation period for the dense phase fluid (Figure 30), it was observed that an advection exists throughout the pipeline, without which the simulation of the phenomena would not be possible. This was previously encountered in [5], where the advection mechanism was in play for column separation during the extended period of shut-in. It was found that the advection mechanism is, in fact, attributed to the diffusion of thermal heat to the surroundings and plays a major role in mass and energy transfer for dense phase fluids. The magnitude of such induced advection is presented via Equation A1.23.

Figure 49 shows the distance plot of Shut-in induced velocity field due to the morning kink-like-behavior on Jun 8, 2022, every 10 minutes between 8:50-10 am.

This is also the cause for the Richardson number exceeding the critical threshold of 0.1 for which the natural convection maybe neglected (see Figure 59).

It's worthwhile remembering that out of the three components present in this pipeline, methane is in its supercritical state and

ethane is compressible liquid below temperature of 32 degrees, and supercritical above 32 C, because the operating pressure of this line is designed to be kept above the critical pressure of ethane of approximately 4.8 MPa. The critical pressure for carbon dioxide is above 7 MPa, therefore in the range of flowing operating condition of this pipeline, carbon dioxide is either liquid, gas or supercritical. The temperature and pressure during the kink-like behavior of the pipeline in shut-in (depicted in Figure 30), confirms that CO₂ can exist in its gaseous phase as the pressure decreases and the temperature increases followed by the collapse of the bubbles as the temperature has been reduced.

The Richardson number helps us understand the transition between forced and free convection, with values below 0.1 indicating forced convection dominance and values above 10 indicating the free convection zone. As observed in the pipeline example, the convection transitions from fully forced to increasingly influenced by free convection due to the movement of gaseous CO₂ in the pipeline.

The abrupt kink discovered during the shut-in period is distinct from the kink observed in the line packing plot. To differentiate it, we first mention the unique characteristics of this newly discovered shut-in kink. Then, we assign a name to it and investigate whether a physical explanation can be found using the same provided model discussed in this paper.

These characteristics distinguish this kink from other abrupt changes in the pressure profile, such as those caused during the propagation of expansion waves of line packing or valve closure.

Hence, we call this previously unanalyzed phenomenon THETA-kink, consists of five letters that describe the significant aspects of the physics of this phenomenon, Thermo-topography (T), Heat transfer (H), Equilibrium (E), Temporal (T), and Advection (A).

By identifying this kink, we can better understand the unique behavior of the pipeline system and potentially improve pipeline management, safety, and leak detection.

The contour plots display the space-time evolution of pressure, velocity, density, and temperature for an entire day during shut-in. From the pressure contours shown in Figures 39, 40, and 41, we can observe changes near the 15th hour, and a closer examination of the top side of the contour presented in Figure 39 reveals another anomaly near 11 AM. By zooming in on these two sides of the space-time contour representation of the pressure, we can see that the first change around 9:50 AM and the second one in the afternoon around 2 PM exhibit local changes compared to their surroundings and their previous values in time.

The temperature contour plot clearly shows that the hottest time of the day on June 8th is between 10 AM and 5 PM. Figure 43

displays the density variations for the same period, revealing significant changes in density at the time of both kinks, the cold kink in the morning and the hot kink in the afternoon, together forming the kink event.

Figure 44 illustrates the space-time contour of velocity, which also demonstrates that the velocities at these two times are at their maximum during shut-in. We reemphasize that this velocity during shut-in is a non-resting standing wave that does not vanish due to density changes inside the pipeline, heat transfer, and constant temperature gradients along and across the pipeline's length.

As shown in Equation A1.23, this velocity can be examined in terms of the convective heat transfer coefficient, Nusselt number, Prandtl number, density, and specific heat at constant pressure. The order of magnitude for this velocity is on the order of centimetres per second. These observations and analyses provide valuable insights into the complex behaviour of pipeline systems during shut-in, which can help improve pipeline management, safety, and leak detection.

ON THE DENSE PHASE LEAK

We previously discussed the importance of simulating dense phase fluids in pipelines near the supercritical point and its relationship with leak detection algorithms. Leakage from a buried pipeline carrying a dense phase can have catastrophic consequences. The subsequent sections delve into the actual physics behind such incidents. Furthermore, we investigated practical leak scenarios in dense phase pipelines, covering catastrophic and controlled fluid withdrawal tests.

Leak tests are classified into various groups, assuming they are conducted as studies rather than in the real physical world. When laboratory tests are not possible, different types of environments may be present when a leak occurs in a pipeline carrying dense phase fluid: air, soil, water (as in the case of NGL being transferred inside a pipeline below sea level), or a controlled process, such as theft or hot tapping. These distinct types of leaks lead to different simulation outcomes and conclusions. We conducted simulated leak test scenarios on a digital twin of an industrial pipeline network, using real-time data for pressure, temperature, and flow rate at both ends of the pipeline, as illustrated in Figure 32.

We prepared leak scenarios for the LDS performance metrics using a USUF thermodynamic approach at the leak location. This approach more closely mimics theft incidents or filling up a tanker. The results indicate that a CPM-based leak detection system can detect pinholes. However, the time window required for a reliable alarm is lengthy unless a novel algorithm used by the CPM-based LDS resolves the causes of delays in the system's response. (For instance, supercriticality, line packing, kink-like behavior, or any other unknown condition with degradation caused inherently by the underlying governing equations that the model solves in real-time) The quantification of the effect of the same issue in slightly compressible liquids

and not a dense phase was discussed in [7]. As it was shown there, lack of knowledge of the density field has consequences on API-1130 metrics performance of CPM-based leak detection systems under the presence of column separation (Also known as slack or cavitation), similar here and due to another type of phase change, another class of degraded operating conditions should have been considered in the design and architecture of CPM models from ground up. The research additionally highlights the susceptibility of pipelines to various types of pin-hole cracks.

The performed analysis showed that there can be pin-holes detectable by an appropriate CPM-based leak detection system (LDS). However, should the leak remain undetected, or the sensitivity of the CPM not be sufficient (for example due to inadequate models of supercritical conditions) the time window required for a reliable alarm to be generated using the provided model seemed to be long. Attention to the following is critical that the speed of sound is around 190m/s for supercritical fluid. This gives a reflection time of greater than 6 minutes. In other words, in 20 echoes of the pressure waves generated from the incident location, the model-based LDS can distinguish it from the ordinary imbalances or transients of the dense phase fluid. Any improvements are limited to the sampling rates and the accuracy of the instruments.

THE MAXIMUM FLOW RATE FROM A CERTAIN HOLE SIZE

The inception of a pinhole can be assumed as an opening in a pressure vessel. Because the diameter of the pipe is much bigger than the diameter of a pinhole leak- or in the case of an arbitrary shape leak the hydraulic diameter of the leak hole is much less than the diameter of the pipe- therefore the leak opening can be assumed as a nozzle with a negative gradient of cross-sectional area to the ambient. Therefore, considering the rupture in a pipeline during shut-in allows us to apply the gas dynamics of nozzle flow.

For homogeneous fluids, this is a known fact that for adiabatic conditions choking occurs with the sonic velocity at the exit plane. However, for dense phase fluids within the vicinity of their supercritical point, this question cannot be answered easily as the properties does not allow for the concept of homogeneity. Given that the maximum velocity that can happen is at the speed of sound, the speed of sound itself depends on highly variable and nonlinear conditions across the supercritical domain, which demands treatment of its own. The acoustic propagation of the speed of sound in the dense phase fluid can be longitudinally variable and highly dependent on temperature as an important parameter. For the hyperbolic type partial differential equations, the numerical condition for stability brings the speed of sound into the numerical discretization of the model. CFL demands dx/dt to be equal to the speed of sound.

The area ratio as a function of the Mach number is discussed, illustrating that the choking condition represents the maximum possible flow rate. This is shown in Figure 64 for different

values of the adiabatic heat index. The difference is that after the choking condition occurs at the throat, here being the cross-section of the hole, the pressure is still too much, compared to the ambient pressure outside, so by a series of expansion waves, the remainder of the pressure loses its value to reach to the ambient pressure. As it can be seen in Figure 64, the ability to expand becomes more and more as the adiabatic heat index increases. The two highest adiabatic heat indices plotted belong to the asymptotic values of the adiabatic heat index at the critical condition which is shown in Figure 12 and Figure 13. As can be seen the maximum value of exit Mach number to the maximum value of adiabatic heat index which according to Figure 13 occurs at the asymptotic value at reduced pressure equal to 1, and this asymptote had been found to be equal to 52.15. The value at the reduced pressure of unity tends to be the maximum theoretical value for a specific heat ratio.

Examining Equation A1.17 reveals a dimensionless ratio between back pressure and stagnation pressure. The occurrence of choking conditions depends on this pressure ratio. If the back pressure to stagnation pressure ratio ($1 / \pi_{0b}$) is greater than one the regime is subsonic (π_{0b} is given by Equation A1.17). If the value is less than one, the ingress phenomenon takes place. Choked supersonic conditions are imminent. As the substance leaks outside, it cannot accelerate beyond the sonic speed across the entire cross-sectional area.

Utilizing Equations A1.16 and A1.17, the formation of choked conditions can be observed, as well as the calculation of choking density, which is also referred to as Sonic stream density. This parameter is significant because, by knowing it and the hole's geometry, the amount of fluid leaking out can be determined.

Figure 65 depicts the pipeline during shut-in, which can be envisioned as a cylindrical reservoir or pressure vessel containing ethane at its stagnation pressure and temperature. The gas is exhausted through a pinhole crack of known diameter or hydraulic diameter (for non-circular shapes) which can be modeled as a simple convergent nozzle.

As discussed earlier, if the total pressure over ambient pressure increases above the critical value, the flow from the pipe to the ambient remains unaffected, as the Mach number stays at the sonic condition of 1 and the total to ambient pressure stays equal to the critical value given by equation A1.17. However, under the conditions shown in Figure 65, the flow tends to expand supersonically, adjusting to ambient pressure through a series of expansion waves and shocks.

Using Figure 66, we can calculate the maximum possible rupture size. Suppose each computational grid point comprises several sections welded together and considering the reaction force from the fluid jets leaking out of the system. In that case, we can imagine that the bending moment of this reaction jet force might reach the yield stress of the pipe material, as demonstrated by the flexure or bending moment equation. We

considered different internal diameters of four and six inches, assuming that sections were 12 meters (40 ft) and 24 meters (80 ft) apart. We regard the provided maximum leak rate as "maximum" because the choking condition at the hole remains valid. The horizontal axis in this figure represents the maximum possible hole size before the reaction of the jet causes irreversible damage to the welding lines.

Figure 67 presents another aspect of this maximum theoretical threshold. We give the maximum fracture or hole size as a function of the adiabatic heat index, which directly affects the speed of sound and, consequently, the amount of matter leaking out of the pipeline. We provide the results for two internal diameters and section lengths.

Figure 68 displays the mass flux of the outgoing dense phase fluid as a function of the adiabatic heat index. The yield stress boundary is depicted by a direct line, illustrating the evolution of detectable pinhole sizes (1/32 inch) up to the onset of yield stress for the entire leaking section.

CONCLUSION

This research delved into supercritical fluid flow in pipelines, specifically under dense phase conditions. The Method of Lines (MOL) was employed to approximate the governing partial differential equation as a system of ordinary differential equations, which were then numerically integrated to yield a numerical solution.

Our findings revealed that the behavior of supercritical fluids strongly depends on their thermodynamic properties, including density, compressibility, and heat capacity. Moreover, the research emphasized the significance of accounting for heat transfer effects when analyzing supercritical flows.

Furthermore, the study explored and discussed line packing and its impact on leak detection. We also investigated the occurrence of kinks in the pipeline during the shut-in period. The results showed that the occurrence of kinks is highly dependent on the pressure and temperature conditions at the pipe ends.

We also investigated the behavior of supercritical fluids during start-up after an extended shut-in period and showed that the density and internal energy of the fluid change rapidly during start-up (Figure 47), and the pressure and temperature distribution along the pipeline exhibit complex behavior.

NOMENCLATURE

PARAMETERS

R	Gas constant
U_{∞}	Overall heat transfer coefficient
k	Thermal conductivity
h_{conv}	Convection heat transfer coefficient
h	Enthalpy (energy equation)
u	Internal energy
q	Heat transfer rate per unit mass
T	Temperature
P	Pressure
V	Velocity
x	Spatial coordinate
t	Time
c_p	Specific heat capacity
m	Mass
A	Pipe cross-section
D	Pipe diameter
L	Pipe length
H	Pipe burial depth
f	friction factor
M	Mach number
E	Pipe Young modulus
D_h	Hole diameter
c	Speed of sound
c_0	Speed of sound in pipe
α	Thermal diffusivity
β	Coefficient of thermal expansion
γ	Heat capacity ratio (Adiabatic heat index)
δ	Wall thickness
ϵ	Roughness
θ	Dimensionless temperature
μ	Viscosity
ν	Kinematic viscosity
ρ	Density
σ	Surface tension
σ_y	Pipe's yield stress
σ_w	Welding yield stress

SUBSCRIPTS

<i>cr</i>	Critical condition
<i>r</i>	Reduced property
<i>c</i>	Characteristic
<i>f</i>	Fluid
<i>l</i>	Liquid
<i>g</i>	Gas
<i>s</i>	Solid
<i>G</i>	Ground
<i>i</i>	Spatial node index
<i>j</i>	Jet reaction force (Eq. A1.28)

DIMENSIONLESS NUMBERS

Nu	Nusselt number	hD/k_f
Bi	Biot number	$h\delta/k_s$
Pr	Prandtl number	$\mu c_p/k$
Re	Reynolds number	$\rho VD/\mu$
Fo	Fourie number	$\alpha t_c/\Delta x^2$
Pe	Peclet number	$Re \cdot Pr$
St	Stranton number	$h/\rho V c_p$
γ	Heat capacity ratio	c_p/c_v
Gr	Grashof number	$g\beta\Delta T D^3/\nu^2$
Ra	Rayleigh number	$Gr \cdot Pr$
Ri	Richardson number	Gr/Re^2
J_H	j-factor for heat transfer	$St \cdot Pr^{2/3}$
We/Bo	Weber/Bond number	$\rho V^2/g\Delta x\Delta\rho$

Dimensionless number- a sample of one set of values

Nu	1260.00
Bi	0.122
Pr	2.530
Re	9E+05
Fo	1E-10
Pe	2E+06
St	7E-04
γ	2.650
Gr	1E+11
Ra	4E+11
Ri	0.158
J_H	0.00121
We/Bo	4E-04

APPENDIX 1- EQUATIONS

$$\frac{\partial \rho}{\partial t} + \frac{\partial(\rho V)}{\partial x} = 0 \quad (\text{A1.1})$$

$$\begin{aligned} \frac{\partial(\rho V)}{\partial t} + \frac{\partial(P + \rho V^2)}{\partial x} \\ = -\frac{f\rho V|V|}{2D} - \rho g \sin \alpha \end{aligned} \quad (\text{A1.2})$$

$$\begin{aligned} \frac{\partial}{\partial t} \left[\left(u + \frac{V^2}{2} \right) \rho \right] + \frac{\partial}{\partial x} \left[\left(h + \frac{V^2}{2} \right) \rho V \right] \\ = \rho q - \rho V g \sin \alpha \end{aligned} \quad (\text{A1.3})$$

$$\frac{dV}{dt} + \frac{1}{\rho} \frac{\partial P}{\partial x} + \frac{fV|V|}{2D} + g \sin \alpha = 0 \quad (\text{A1.4})$$

$$\rho \frac{dh}{dt} - \frac{dP}{dt} - \frac{f\rho V^3}{2D} = \rho q \quad (\text{A1.5})$$

$$dh = c_p dT + \left[1 + \frac{T}{\rho} \left(\frac{\partial \rho}{\partial T} \right)_P \right] \frac{dP}{\rho} \quad (\text{A1.6})$$

$$\frac{1}{Fo} \frac{\partial T}{\partial t} = \frac{\partial^2 T}{\partial x^2} - (Nu)(T - T_\infty) \quad (\text{A1.7})$$

$$P = Z\rho RT \quad (\text{A1.8})$$

$$c_g = \sqrt{\frac{B}{\rho}} \quad , B = \gamma P \quad (\text{A1.9})$$

$$c_0 = \sqrt{\frac{1}{\rho \left(\frac{1}{B} + \frac{D}{E\delta_{th}} \right)}} \quad (\text{A1.10})$$

$$T_t/T = \left(1 + \frac{\gamma-1}{2} M^2 \right) \quad (\text{A1.11})$$

$$P_t/P = \left(1 + \frac{\gamma-1}{2} M^2 \right)^{\frac{\gamma}{\gamma-1}} \quad (\text{A1.12})$$

$$\rho_t/\rho = \left(1 + \frac{\gamma-1}{2} M^2 \right)^{\frac{1}{\gamma-1}} \quad (\text{A1.13})$$

$$A^*/A = M \left(\frac{\frac{\gamma+1}{2}}{1 + \frac{\gamma-1}{2} M^2} \right)^{\frac{(\gamma+1)}{2(\gamma-1)}} \quad (\text{A1.14})$$

$$M = \frac{\dot{m} \sqrt{R T_t/\gamma}}{A P_t \left(1 + \frac{\gamma-1}{2} M^2 \right)^{\frac{0.5(1+\gamma)}{1-\gamma}}} \quad (\text{A1.15})$$

$$\pi_{CD} = \left(\frac{2}{\gamma+1} \right)^{\frac{\gamma+1}{2(\gamma-1)}} \quad (\text{A1.16})$$

$$\pi_{ob} = \left(\frac{\gamma+1}{2} \right)^{\frac{\gamma}{\gamma-1}} \quad (\text{A1.17})$$

$$\dot{m} = \sqrt{\gamma/RT} (PMA) \quad (\text{A1.18})$$

$$R_{eq} = \left(\frac{R_1 R_2 R_3}{R_1 + R_2 + R_3} \right) \parallel \left(R_w + \frac{R_G R_{rad}}{R_G + R_{rad}} \right) \quad (\text{A1.19})$$

$$R_G = \left(\frac{1}{2\pi k_G} \right) \ln \left(\frac{H}{D} + \sqrt{\left(\frac{H}{D} \right)^2 - 1} \right) \quad (\text{A1.20})$$

$$err(T_G = constant) \leq 1 - erf \left(\frac{H}{2\sqrt{at}} \right) \quad (\text{A1.21})$$

$$\frac{T_{i+1} - T_G}{T_i - T_G} = exp \left(-\frac{U_\infty (\pi D \Delta x)}{\dot{m} c_p} \right) \quad (\text{A1.22})$$

$$V_{Shut-In} = \frac{h \cdot Nu \cdot Pr^{0.233}}{0.121 \rho c_p} \quad (\text{A1.23})$$

$$\dot{m}^* = \rho c_0 \pi_{CD} A^* \quad (\text{A1.24})$$

$$h_{loss} = \frac{4}{5} \frac{f \Delta x}{g D^5} \left(\frac{\dot{m}}{\rho_i} \right)^2 \quad (\text{A1.25})$$

$$Nu = 0.023 Re^{0.8} Pr^{0.3} \quad (\text{A1.26})$$

$$M_e = \left[\left(\frac{2}{\gamma-1} \right) \left((\pi_{ob})^{\frac{\gamma-1}{\gamma}} - 1 \right) \right]^{1/2} \quad (\text{A1.27})$$

$$F_j = \dot{m}_j c_0 \quad (\text{A1.28})$$

$$\dot{m}_{leak} \geq \frac{\pi D^3 \sigma_y}{16 c_0 L_{section}} \quad (\text{A1.29})$$

$$D_h \geq \frac{D}{2c_0} \sqrt{\frac{D}{L_{section}} \frac{\sigma_w}{\rho_0 \pi CD}} \quad (\text{A1.30})$$

$$\Delta P = \rho c_0 \Delta V \quad (\text{A1.31})$$

$$\frac{V_6''}{V_4''} = \sqrt{\frac{f_4'' D_6''}{f_6'' D_4''}} \quad (\text{A1.32})$$

$$\frac{1}{c_0^2} \frac{\partial P}{\partial t} + \frac{\partial(\rho V)}{\partial x} = \sigma \quad (\text{A1.33})$$

$$\frac{D(\rho V)}{Dt} + \frac{\partial P}{\partial x} + \frac{(\rho_l - \rho_v)^2 \rho_l f^*}{2D(\rho - \rho_v)} V|V| + \rho f_x - \beta = 0 \quad (\text{A1.34})$$

$$\tau_t = \frac{\rho c_p \forall}{U_\infty A}, A = \pi D \Delta x \quad (\text{A1.35})$$

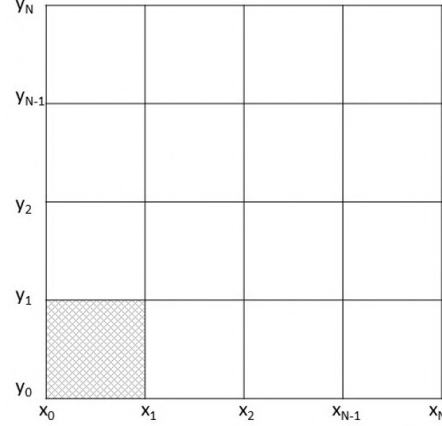
$$\tau_t = R_t C_t, R_t = \frac{1}{U_\infty} \quad (\text{A1.36})$$

$$2\tau_t \alpha \Delta t \leq 2\tau_t \Delta x^2 - \Delta t \Delta x^2 \quad (\text{A1.37})$$

$$Fo \leq \frac{1}{2} \leftrightarrow \frac{\alpha \Delta t}{\Delta x^2} \leq \frac{1}{2} \rightarrow \frac{\alpha}{c_0 \Delta x} \leq \frac{1}{2} \quad (\text{A1.38})$$

$$\hookrightarrow \Delta x \geq \frac{2\alpha}{c_0} \rightarrow \Delta x \geq \sqrt{2\alpha \Delta t}$$

APPENDIX 2- TRANSFINITE INTERPOLATION



Use this schematic for the Transfinite Interpolation on the edges:

$$\Phi_0(x) = \frac{x_1 - x}{x_1 - x_0} \quad (\text{A2.1})$$

$$\Phi_1(x) = \frac{x_0 - x}{x_0 - x_1} \quad (\text{A2.2})$$

$$\Psi_0(y) = \frac{y_1 - y}{y_1 - y_0} \quad (\text{A2.3})$$

$$\Psi_1(y) = \frac{y_0 - y}{y_0 - y_1} \quad (\text{A2.4})$$

$$\begin{aligned} F(x, y) &= \sum_{m=0}^M \Phi_m(x) F(x_m, y) \\ &+ \sum_{n=0}^N \Psi_n(y) F(x, y_n) \\ &- \sum_{m=0}^M \sum_{n=0}^N \Phi_m(x) \Psi_n(y) F(x_m, y_n) \end{aligned} \quad (\text{A2.5})$$

$$\Phi_m(x) = \prod_{k=0, k \neq m}^M \frac{x - x_k}{x_m - x_k} \quad (\text{A2.6})$$

$$\Psi_n(y) = \prod_{k=0, k \neq n}^N \frac{y - y_k}{y_n - y_k} \quad (\text{A2.7})$$

REFERENCES

- [1] Gorelli, F., Bryk, T., Krisch, M. et al. (2013). Dynamics and Thermodynamics beyond the critical point. *Scientific Reports*, 3, 1203.
- [2] Friend, D. G., Ely, J. F., & Ingham, H. (1993). Tables for the Thermophysical Properties of Ethane. National Institute of Standards and Technology Technical Note.
- [3] American Petroleum Institute. (1995). API 1155: Evaluation Methodology for Software Based Leak Detection Systems. 1st Edition.
- [4] American Petroleum Institute. (2002). API 1130: Computational Pipeline Monitoring for Liquid Pipelines. 2nd Edition.
- [5] Ghasvari Jahromi, H., Roxas, M., & Mokamati, S. (2018). Column Separation in a Shut-In Liquid Hydrocarbon Transmission Pipeline. Proceedings of the 12th International Pipeline Conference, Calgary, Alberta, Canada. IPC2018-78743.
- [6] Ghasvari Jahromi, H., Ekram, F., Roxas, M., & Mokamati, S. (2019). A Mathematical Model for the Spatial Prediction and Temporal Evolution of the Column Separation in a Flowing Hydrocarbon Transmission Pipeline. Paper presented at the PSIG Annual Meeting, London, UK. PSIG-1910.
- [7] Ghasvari Jahromi, H., Ekram, F., Ali, W., Roxas, M., & Mokamati, S. (2021). Performance of CPM Based Leak-Detection Algorithms in the Presence of Slack. Paper presented at the PSIG Annual Meeting, Virtual. PSIG-2103.
- [8] M. J. Zucrow and J. D. Hoffman, "Gas dynamics", Vol. 1 and 2, J. Wiley, 1976.
- [9] Chaczykowski, M., & Osiadacz, A. J. (2012). Dynamic simulation of pipelines containing dense phase/supercritical CO₂-rich mixtures for carbon capture and storage. *International Journal of Greenhouse Gas Control*, 9, 446-456.
- [10] Flatt, R. (1986). Unsteady compressible flow in long pipelines following a rupture. *International Journal for Numerical Methods in Fluids*, 6(2), 83-100.
- [11] Shojaeefard, M., Goudarzi, K., & Jahromi, H. G. (2007). Numerical Simulation of 2-D Turbidity Currents and Wall Jet. *American Journal of Applied Sciences*, 4(11), 880-886.

AUTHOR BIOGRAPHY

Hamed Ghasvari Jahromi is a leading Chief R&D Scientist at Vanmok Leak Detection Technologies Inc., with over 12 years of experience in computational fluid dynamics and mathematical modeling. His Ph.D. research at the University of British Columbia focused on the mathematical modeling of multiphase flows. Hamed has worked across various industries, including oil and gas, chemical, and petrochemical. He holds a patent for predicting pipeline column separations and has published numerous research articles. Hamed's expertise lies in leak detection technologies, column separation prediction models, Real-Time Transient Model (RTTM), and pattern recognition approaches.

Fatemeh Ekram is an R&D scientist at Vanmok Leak Detection Technologies Inc. She has extensive expertise in process simulation, optimization, and control. Over the past 5 years, her focus was on developing leak detection algorithms using a combination of model-based and data-driven techniques. Fatemeh got her B.Sc. and M.Sc. degrees from the Sharif University of Technology and her Ph.D. in Chemical & Biological Engineering from the University of British Columbia in 2016.

Chuntao Deng was Pipeline Integrity Specialist at Keyera Corp., in Calgary, Alberta, Canada between 2014 and 2022. He has over 18 years of experience in pipeline corrosion control, pipeline release, risk modeling, and integrity management. He has a Ph.D. degree in Chemical Engineering from the University of British Columbia, BC, and is a registered Professional Engineer in Alberta, Canada

Jim Knudson has worked as a Leak detection Specialist for the last 13 years, 5 years at Enbridge Pipeline, 2.5 years at Spectra Energy, 4 years at Vanmok Consulting, and 1.5 years at Keyera Energy. Previous to this discipline Jim worked at Enbridge Pipeline as a Pipeline Operator for 20 years.

Satya Mokamati is the President & CEO of Vanmok Leak Detection Technologies Inc. He is a professional engineer with over 15 years of experience in the oil and gas sector, with in-depth industry knowledge. Prior to founding Vanmok, Satya worked as a subject matter expert in pipeline leak detection at a major midstream pipeline company. Satya holds a Ph.D. in Mechanical Engineering from UBC, Vancouver, and an MS in Mechanical Engineering from UNB, Fredericton. He is a member of APEGA and is dedicated to advancing leak detection technology in the pipeline industry.

FIGURES

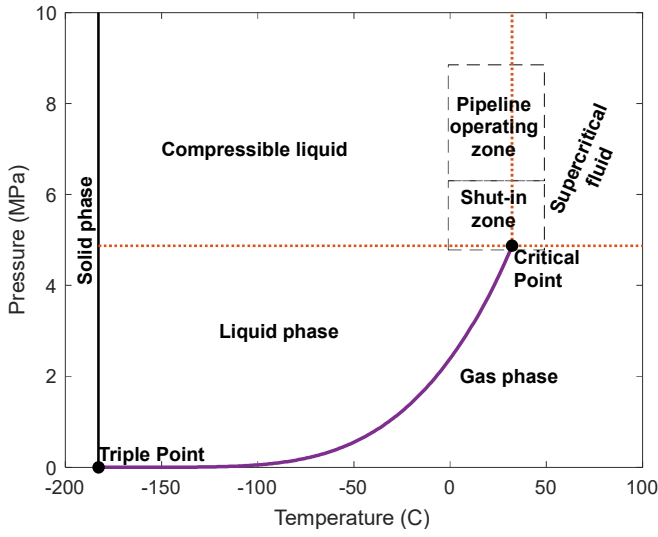


Figure 1- Ethane phase diagram showing the pipeline operating and shut-in temperature and pressure ranges.

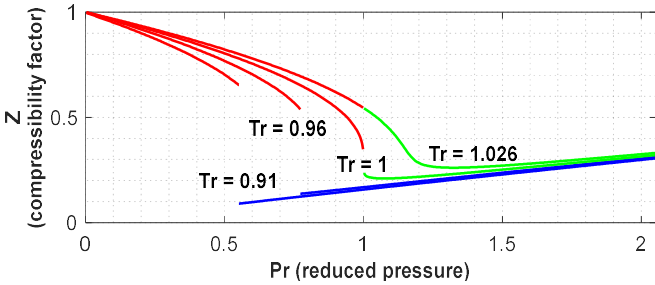


Figure 2- Compressibility factor vs reduced pressure at different temperatures (liquid, gas and supercritical states are represented in blue, red and green respectively).

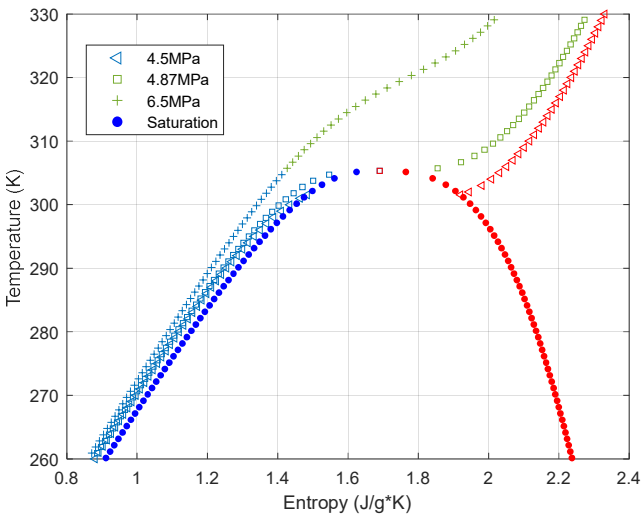


Figure 3- Ethane T-S diagram.

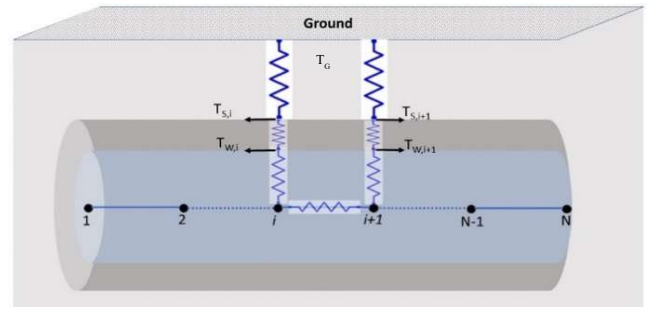


Figure 4- Thermal layers considered to calculate the overall heat transfer coefficient. T_G , T_S , and T_W correspond to the ground, pipe's skin, and wall.

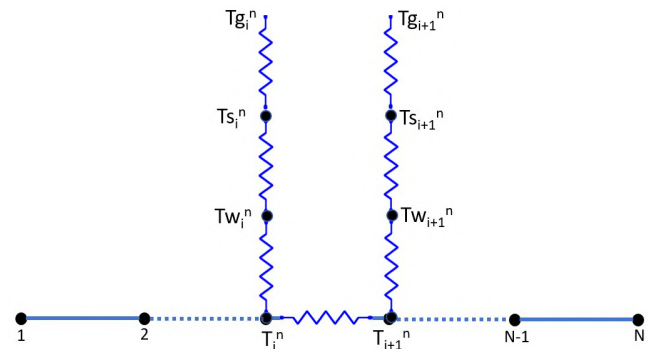


Figure 5- The composite structure of a typical transmission pipeline showing the layers of the pipe wall, insulation, and ground.

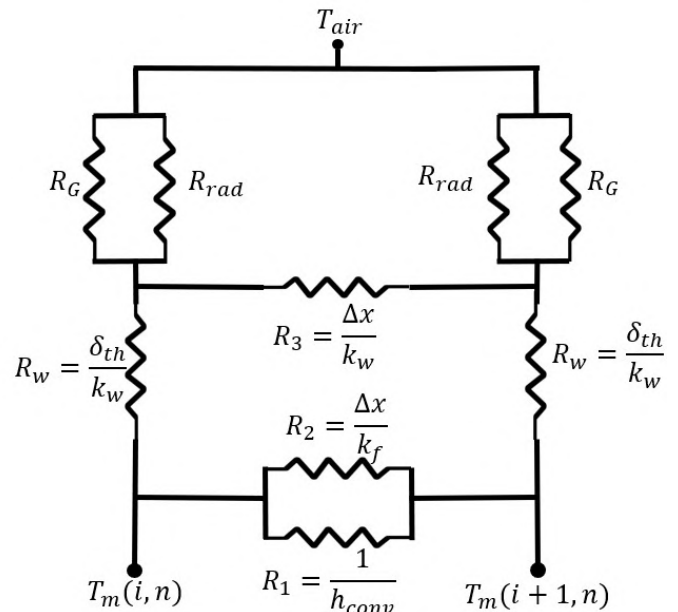


Figure 6- Heat transfer resistances (i is the spatial node index and n is the time step index).

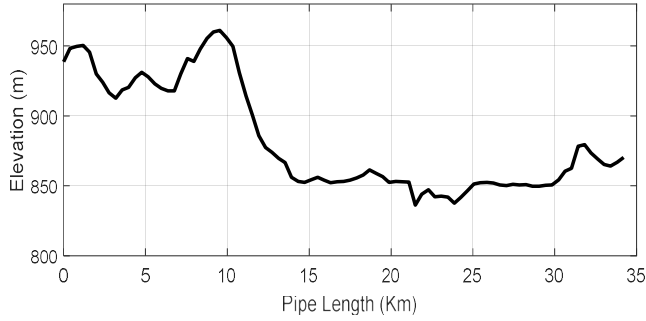


Figure 7- Pipeline elevation profile.

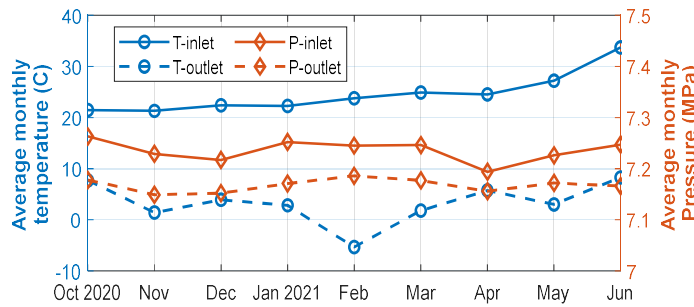


Figure 8- Average monthly operating temperature and pressure.

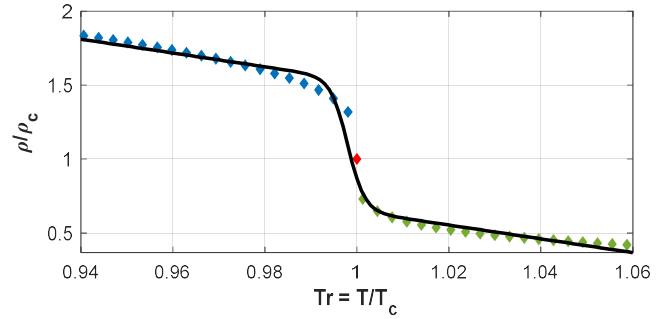


Figure 10- Reduced density vs reduced temperature at P_{cr} (dots) and the fitted curve (solid line).

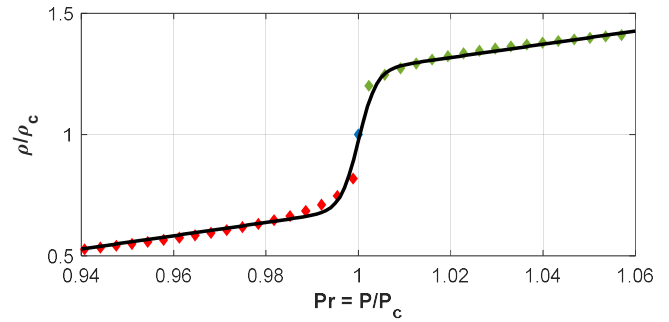


Figure 11- Reduced density vs reduced pressure at T_{cr} (dots) and the fitted curve (solid line).

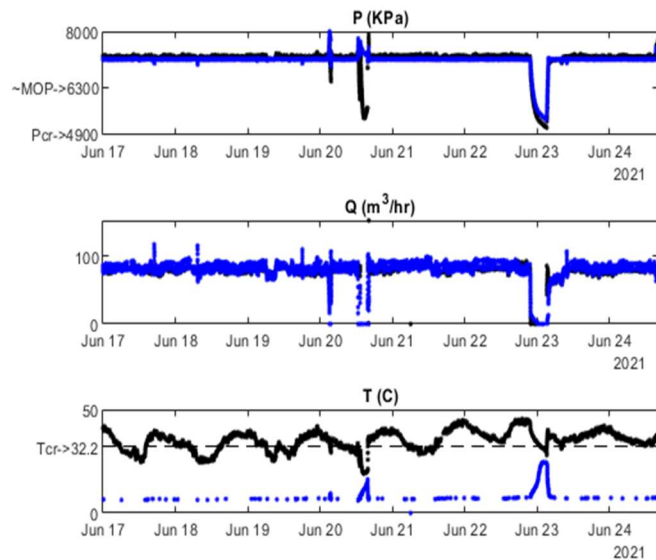


Figure 9- An example of the supercritical operating condition (inlet: black line, outlet: blue line).

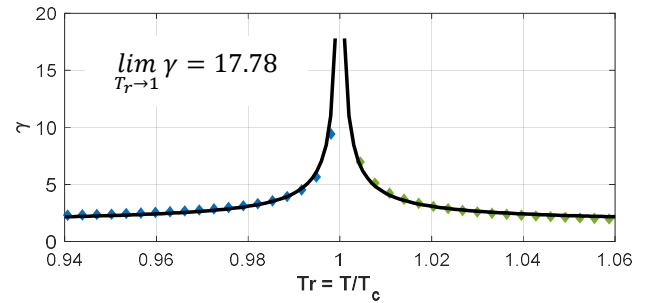


Figure 12- Heat capacity ratio vs reduced temperature at P_{cr} (dots) and the fitted curve (solid line).

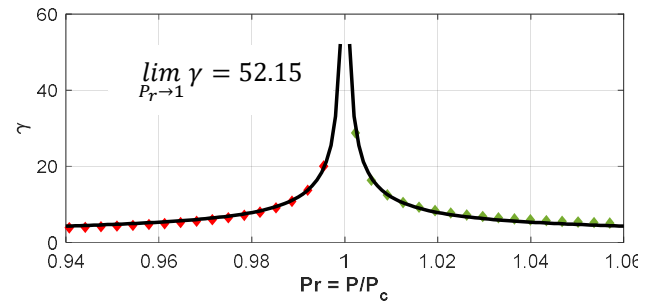


Figure 13- Heat capacity ratio vs reduced temperature at T_{cr} (dots) and the fitted curve (solid line).

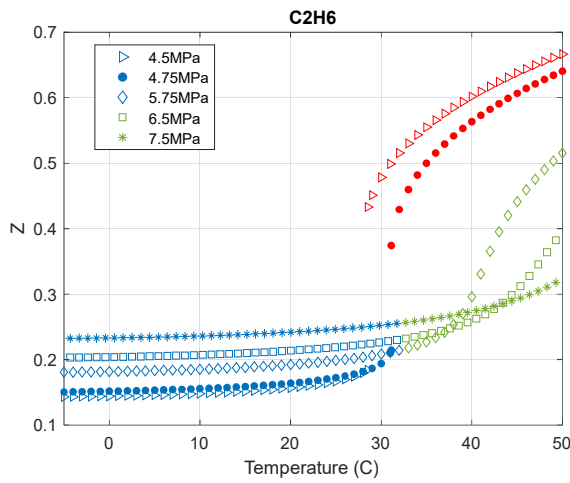


Figure 14- Ethane compressibility factor for different temperatures and pressures (liquid, gas and supercritical states are represented in blue, red and green respectively).

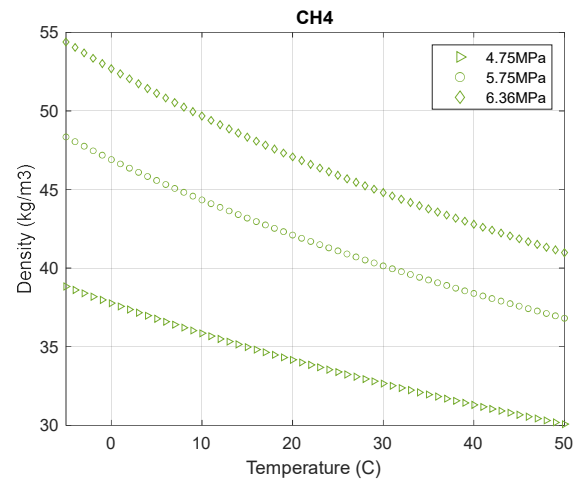


Figure 17- CH4 density for different temperatures and pressures (liquid, gas, and supercritical states are represented in blue, red and green respectively).

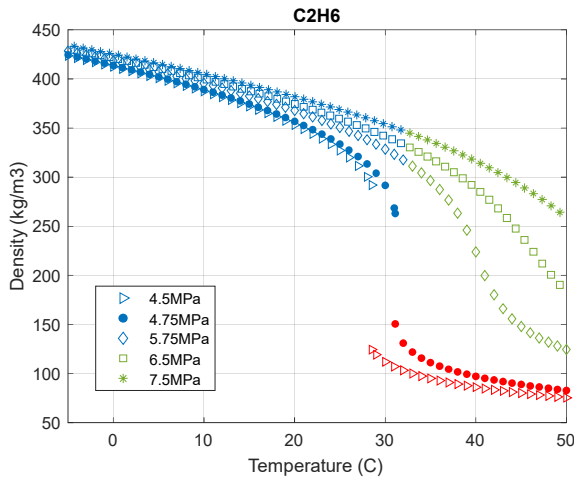


Figure 15- Ethane density for different temperatures and pressures (liquid, gas, and supercritical states are represented in blue, red and green respectively).

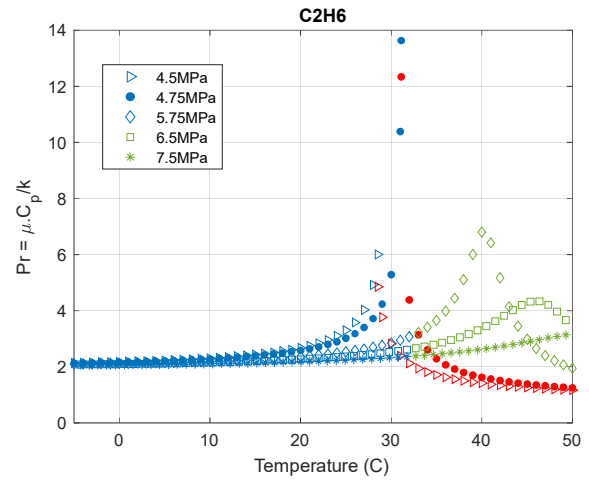


Figure 18- Ethane Prandtl number for different temperatures and pressures (liquid, gas and supercritical states are represented in blue, red and green respectively).

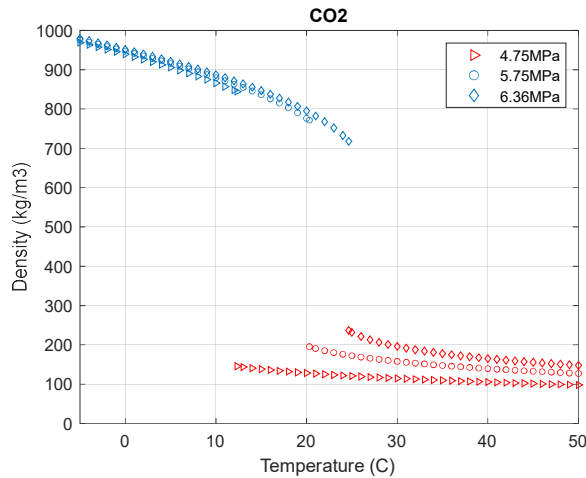


Figure 16- CO2 density for different temperatures and pressures (liquid, gas, and supercritical states are represented in blue, red and green respectively).

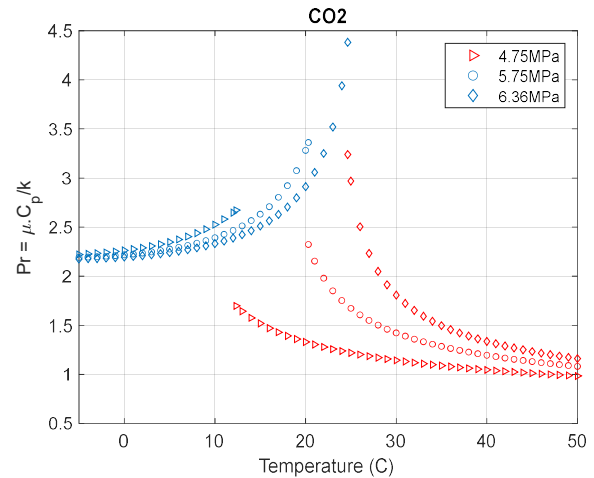


Figure 19- CO2 Prandtl number for different temperatures and pressures (liquid, gas and supercritical states are represented in blue, red and green respectively).

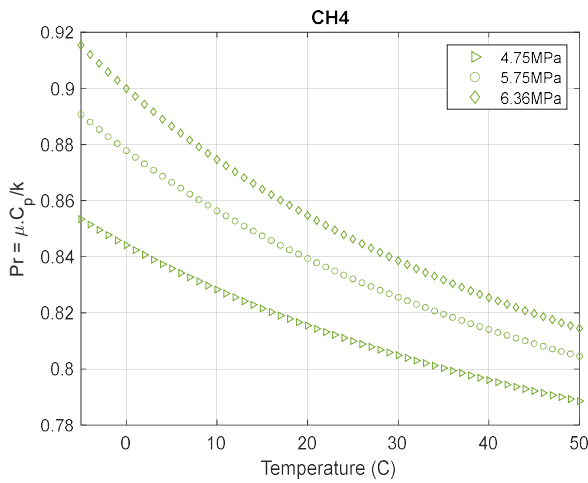


Figure 20- CH4 Prandtl number for different temperatures and pressures (liquid, gas and supercritical states are represented in blue, red and green respectively).

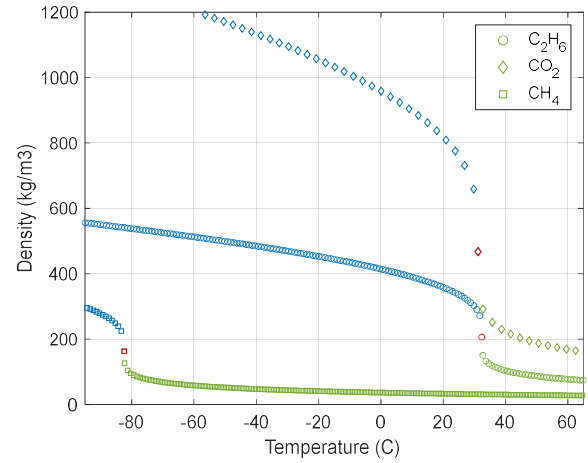


Figure 23- Density of main components at their P_{cr} (liquid, gas, and supercritical states are represented in blue, red and green respectively).

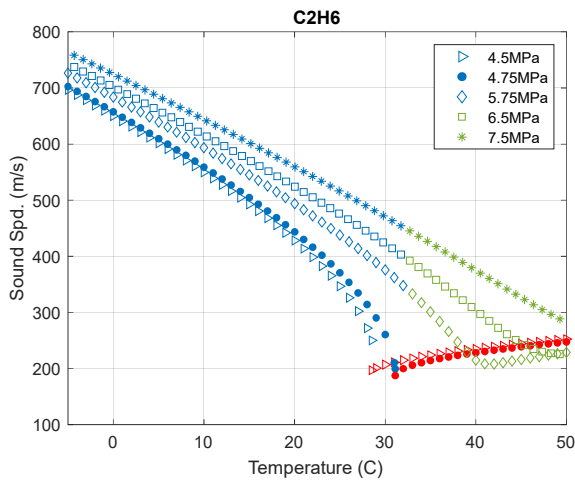


Figure 21- C2H6 Speed of sound for different temperatures and pressures (liquid, gas and supercritical states are represented in blue, red and green respectively).

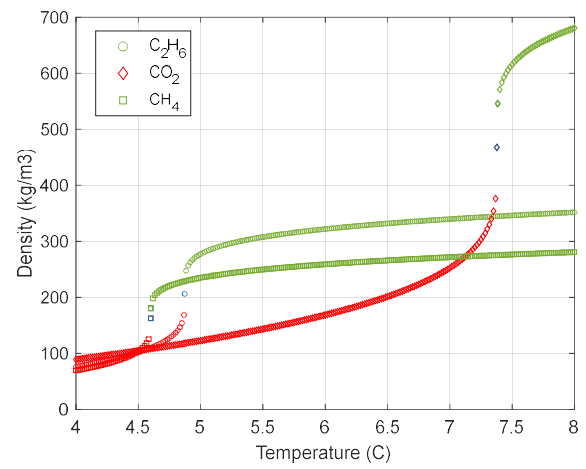


Figure 24- Density of main components at their T_{cr} (liquid, gas, and supercritical states are represented in blue, red and green respectively).

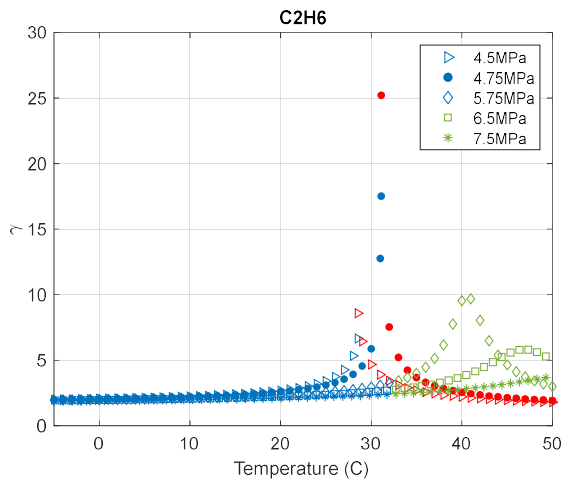


Figure 22- Ethane heat capacity ratio for different temperatures and pressures (liquid, gas and supercritical states are represented in blue, red and green respectively).

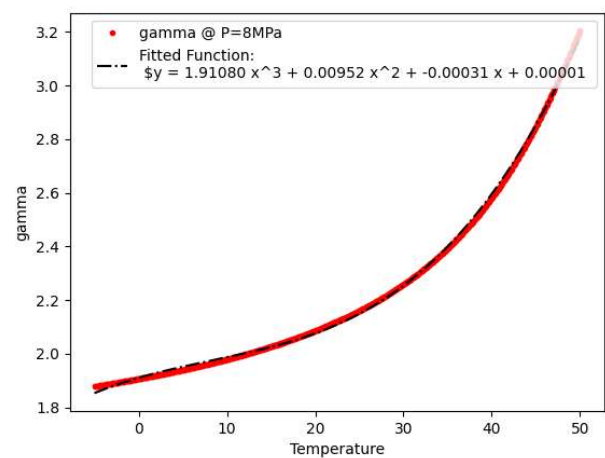


Figure 25- Fitted curve for adiabatic heat index vs temperature at $P=8\text{MPa}$.

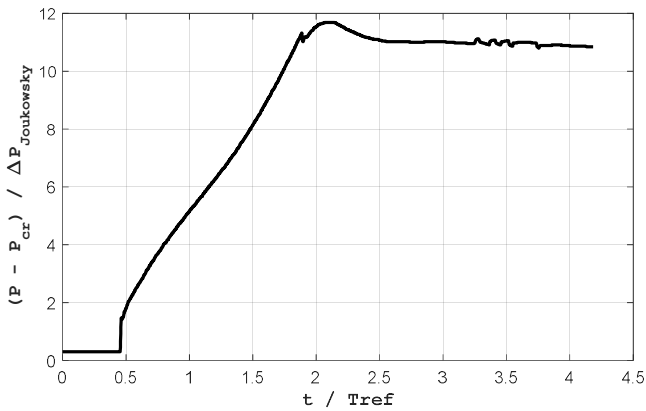


Figure 26- Dimensionless pressure vs dimensionless time showing line packing.

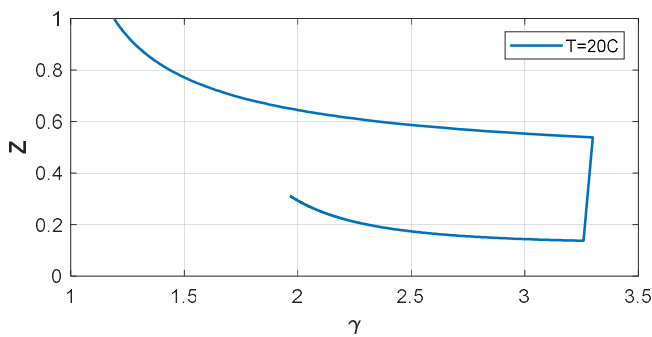


Figure 27- Compressibility factor vs heat capacity ratio at 20C.

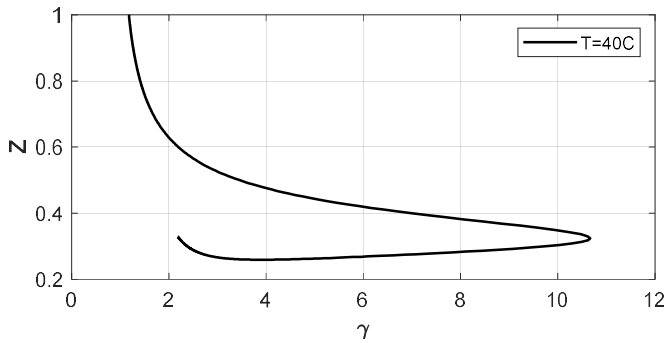


Figure 28- Compressibility factor vs heat capacity ratio at 40C.

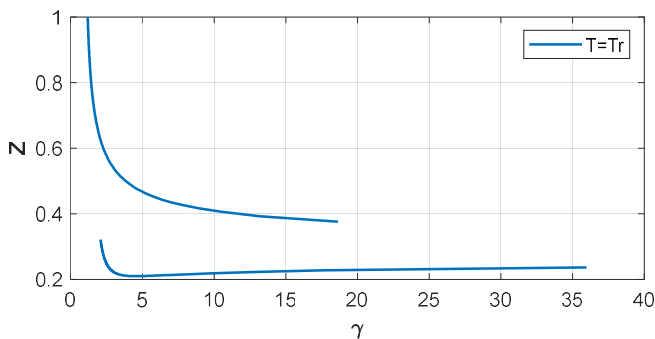


Figure 29- Compressibility factor vs heat capacity ratio at critical temperature.

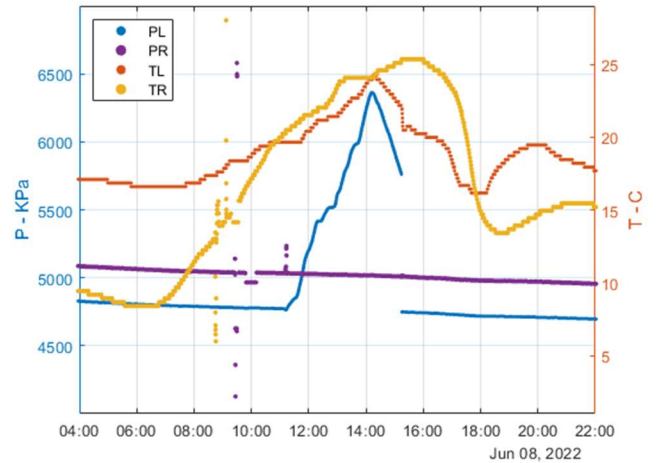


Figure 30- Pressure (left) and temperature (right) of the pipe ends for the occurrence of the kinks during the shut-in period.

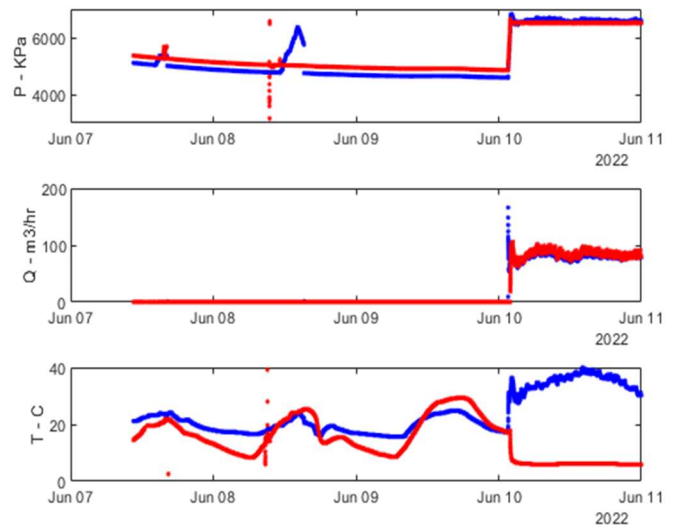


Figure 31- Pressure (top), flow rate (middle) and temperature (bottom) at the pipe ends for the extended shut-in period followed by the line start-up.

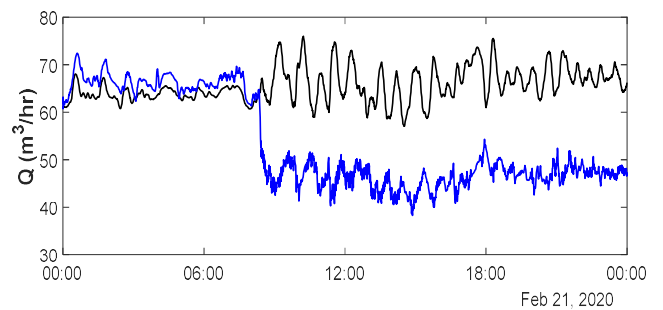


Figure 32- Simulated leak test on 6-inch branch. (USUF)

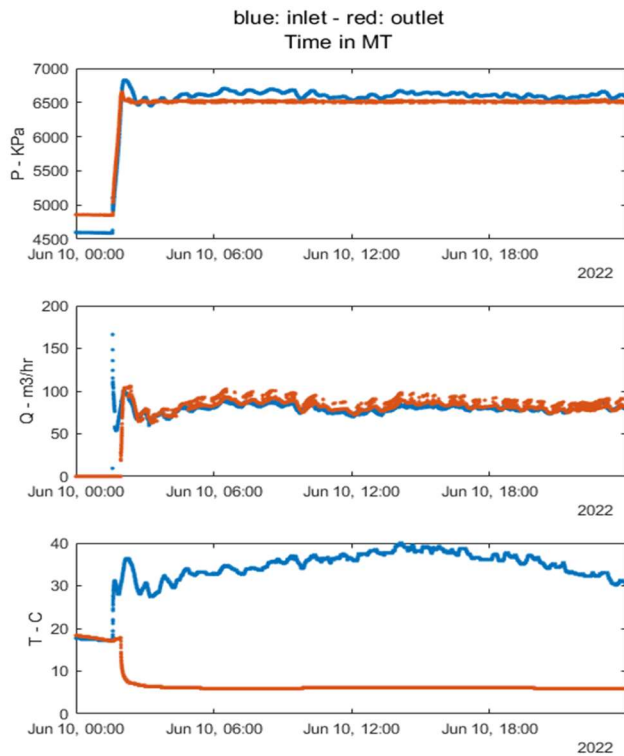


Figure 33- Pressure (top), flow rate (middle) and temperature (bottom) at the pipe ends as the fluid goes into its supercritical state at the inlet.

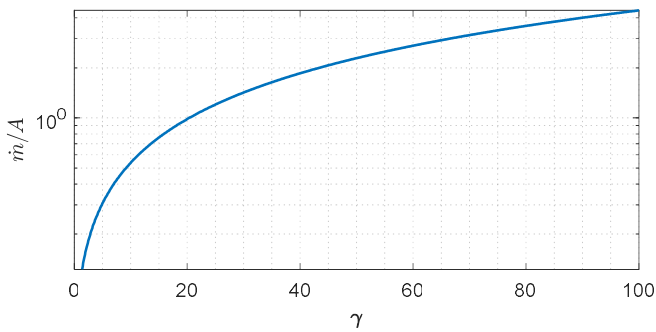


Figure 34- Mass flow rate over cross section area vs γ .

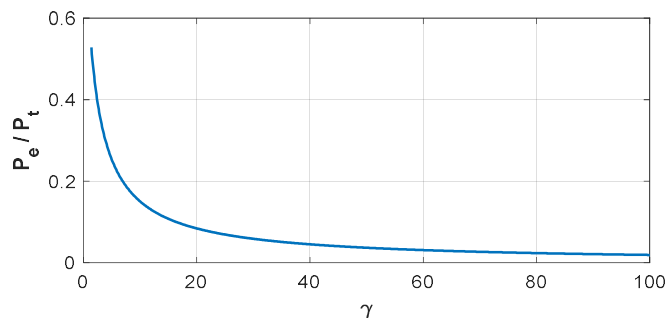


Figure 35- P_e / P_t vs γ ($1/\pi_{0b} = P_e / P_t$).

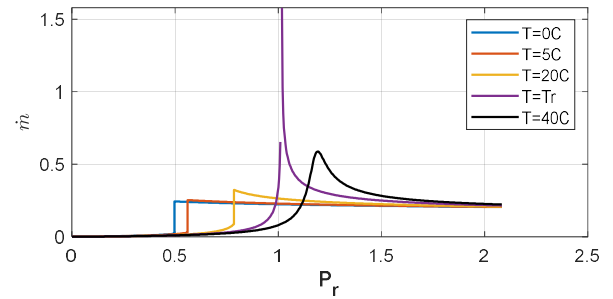


Figure 36- Mass flow rate vs reduced pressure at different temperatures.

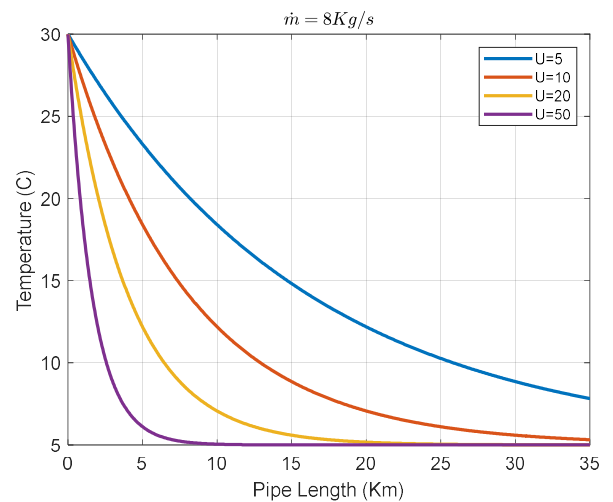


Figure 37- Temperature changes along the pipe for different overall heat transfer coefficient

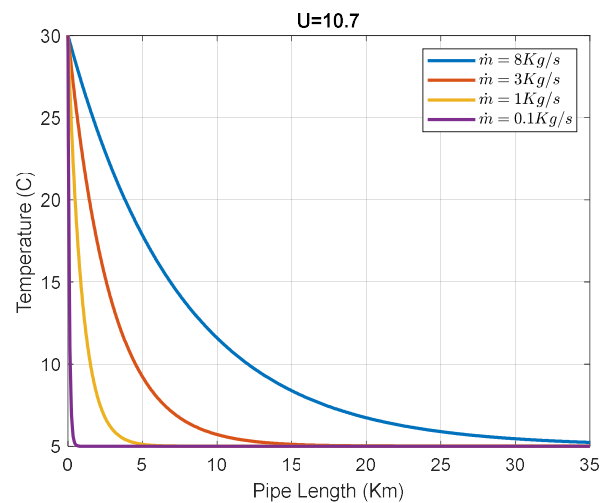


Figure 38- Temperature changes along the pipe for different mass flow rates.

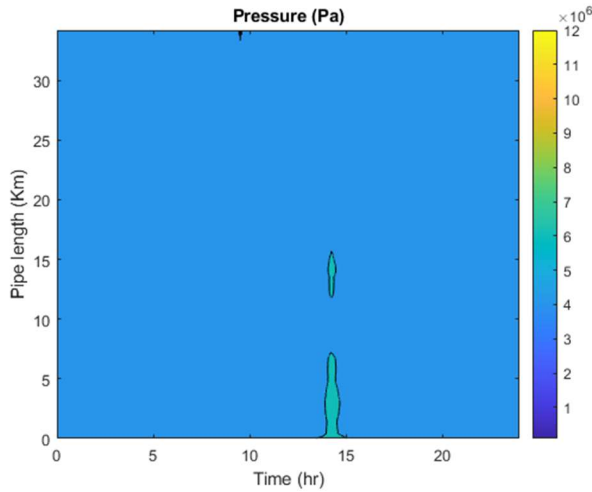


Figure 39- Pressure contour for Shut-in period (Jun 8, 2022).

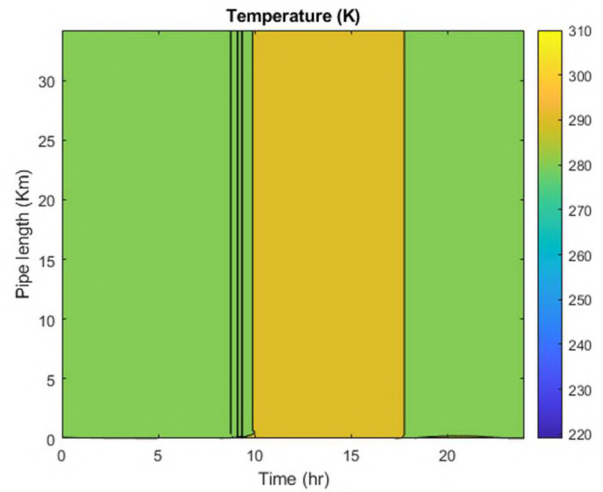


Figure 42- Temperature contour for Shut-in period (Jun 8, 2022).

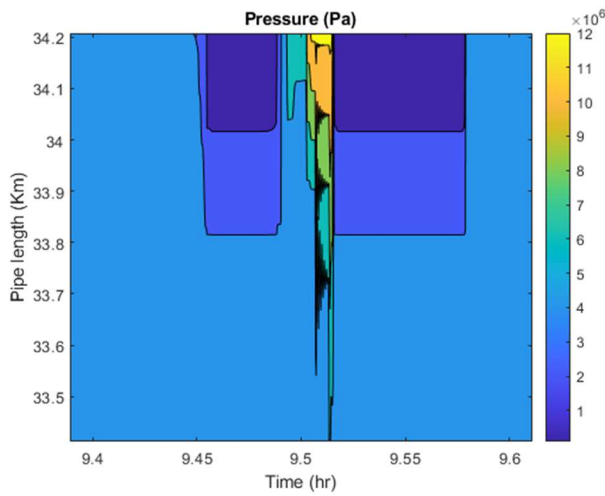


Figure 40- Pressure contour for Shut-in period (Jun 8, 2022), zoomed to show the morning event.

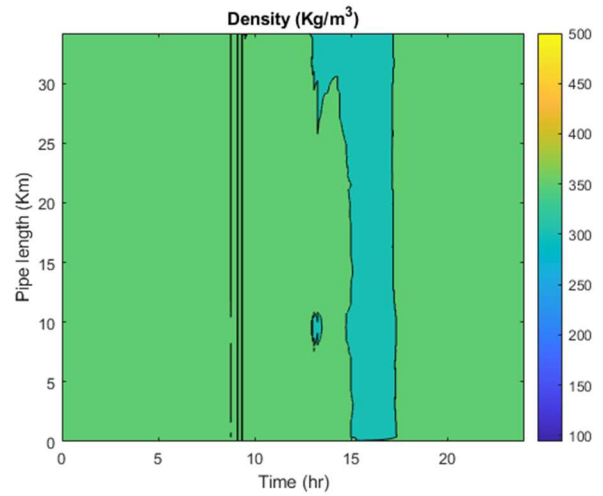


Figure 43- Density contour for Shut-in period (Jun 8, 2022).

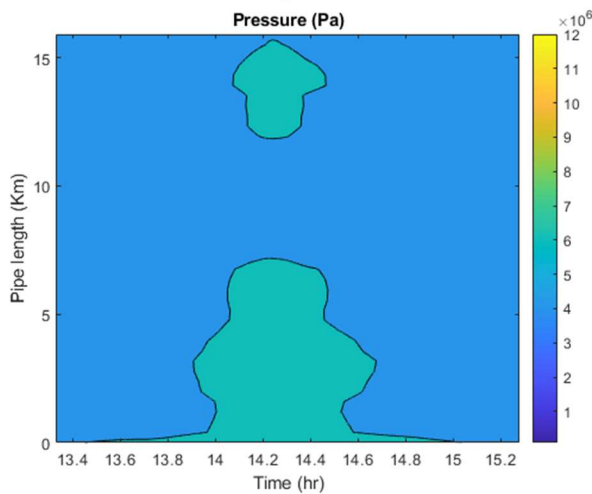


Figure 41- Pressure contour for Shut-in period (Jun 8, 2022), zoomed to show the afternoon event.

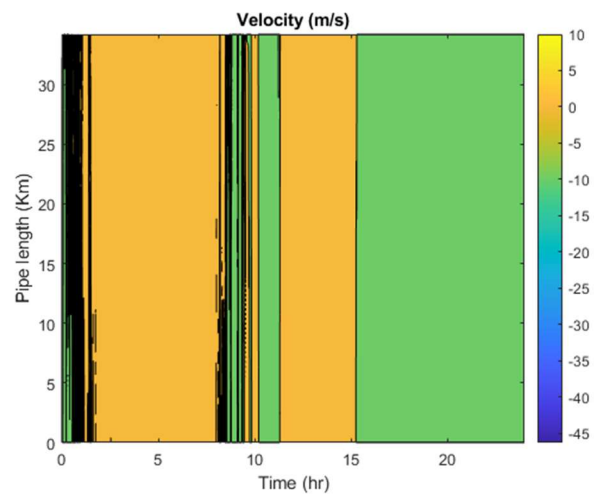


Figure 44- Velocity contour for Shut-in period (Jun 8, 2022).

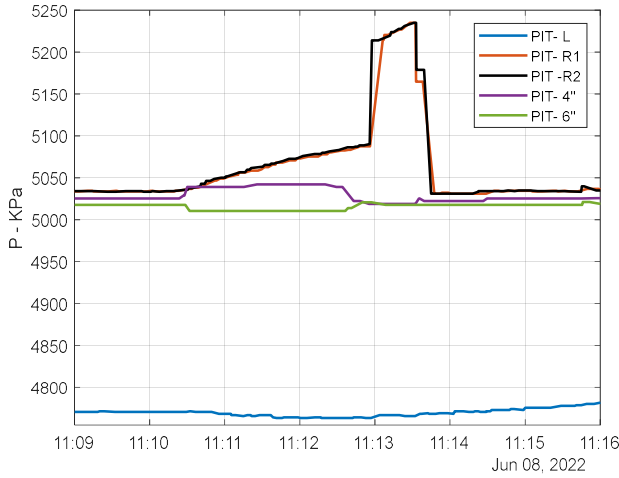


Figure 45- Pressure transmitter readings for the shut-in period as the line warms up during the day.

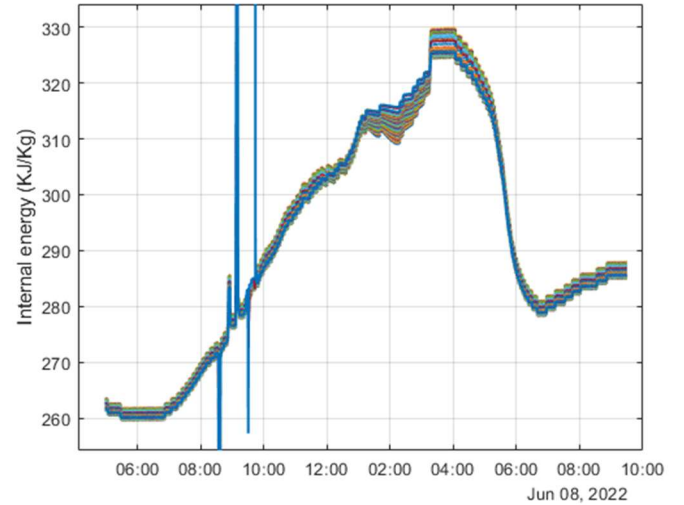


Figure 48- Internal energy changes vs time for internal nodes showing both morning and afternoon kink-like behavior.

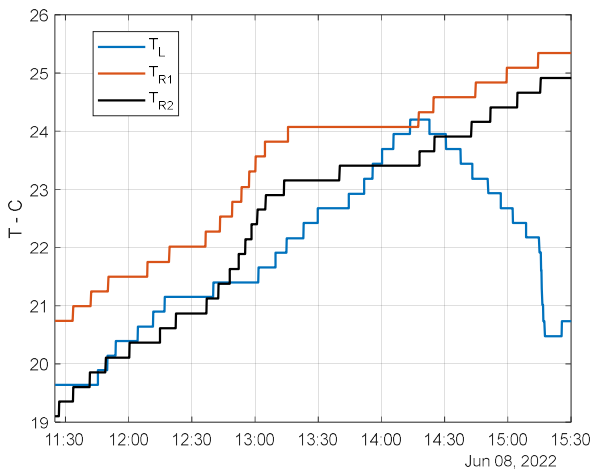


Figure 46- Temperature transmitter readings for the shut-in period as the line warms up during the day.

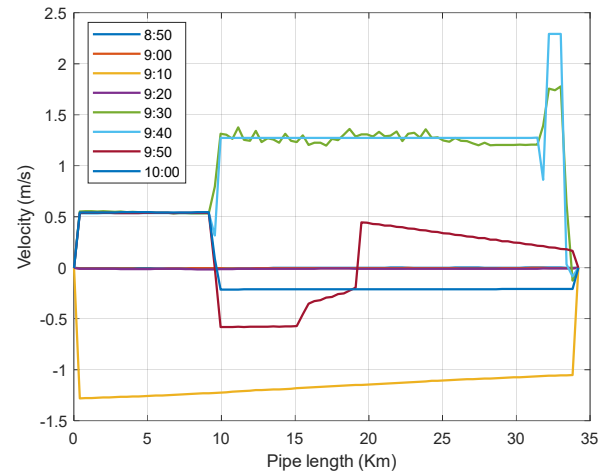


Figure 49- Distance plot of Shut-in induced velocity field due to the morning kink-like-behavior on Jun 8, 2022, every 10 minutes between 8:50-10 am.

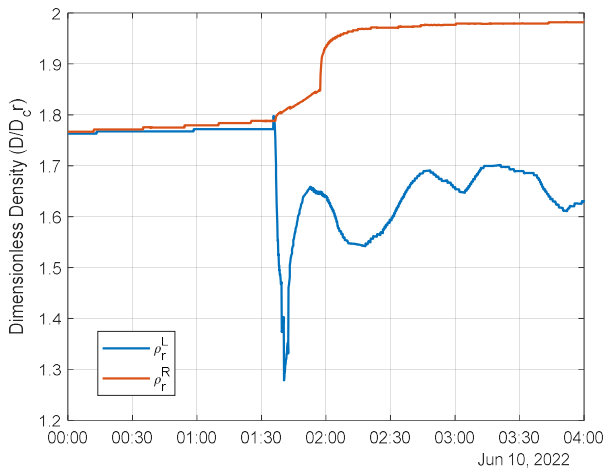


Figure 47- reduced density vs time during the line start-up after 3 days of shut-in.

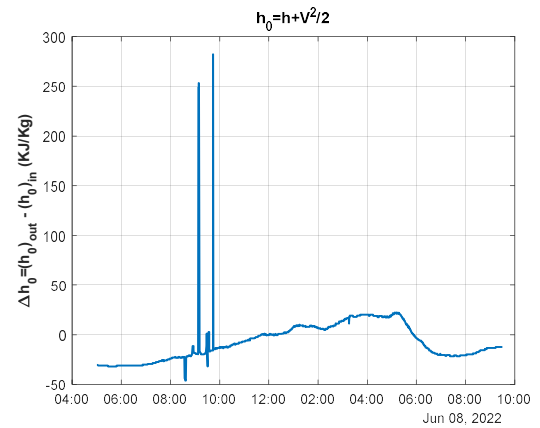


Figure 50- Changes in stagnation enthalpy with time during shut-in.

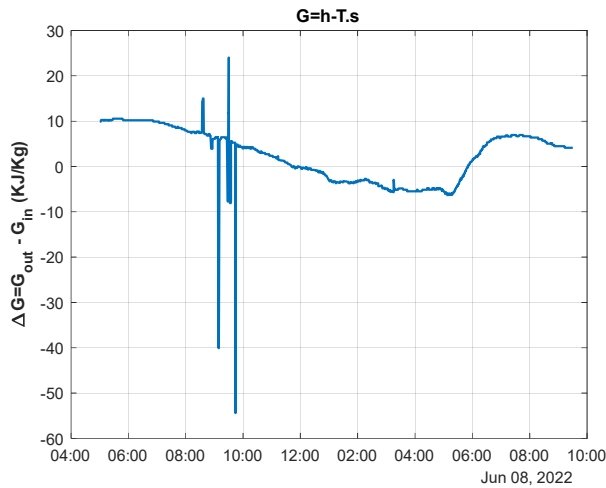


Figure 51- Changes in Gibbs free energy with time for shut-in.

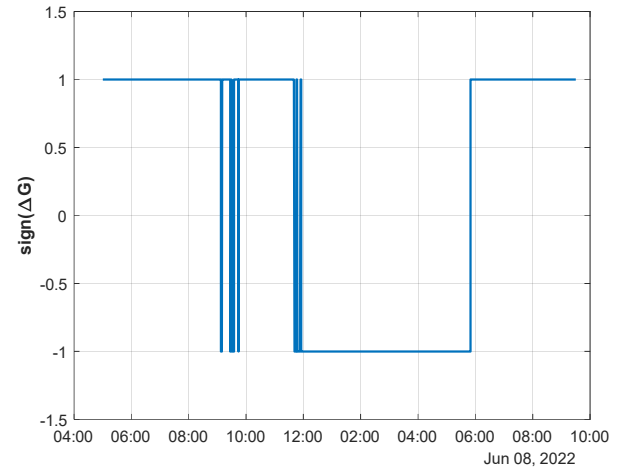


Figure 54- Changes in the sign of ΔG during shut-in.

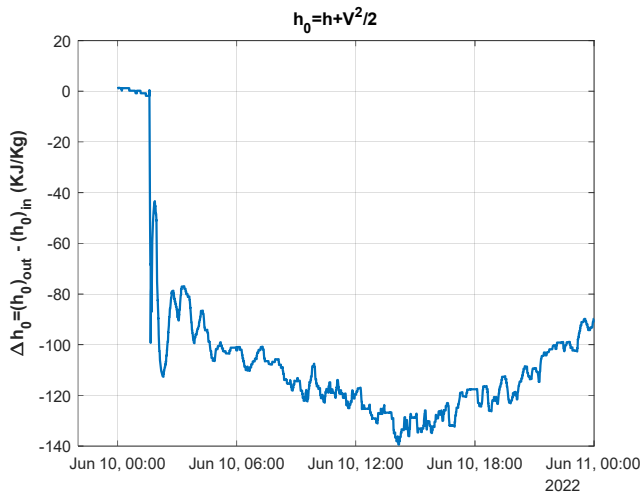


Figure 52- Changes in stagnation enthalpy with time as the line starts up after 3 days of shut-in.

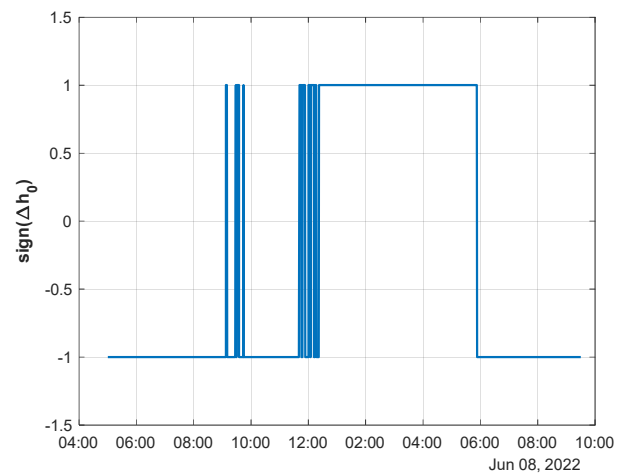


Figure 55- Changes in the sign of Δh_0 during shut-in.

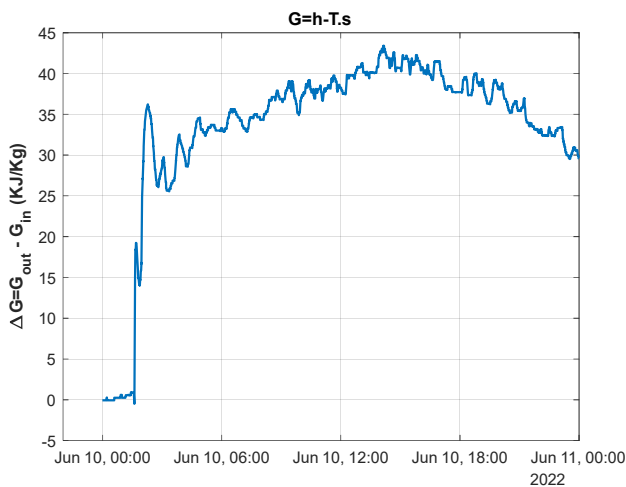


Figure 53- Changes in Gibbs free energy with time as the line starts up after 3 days of shut-in.

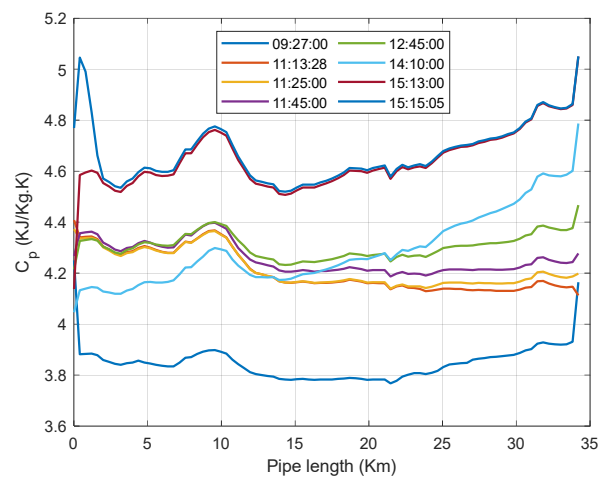


Figure 56- Distance plot of Cp for different times during the kink-like-behavior of 8 June 2022.

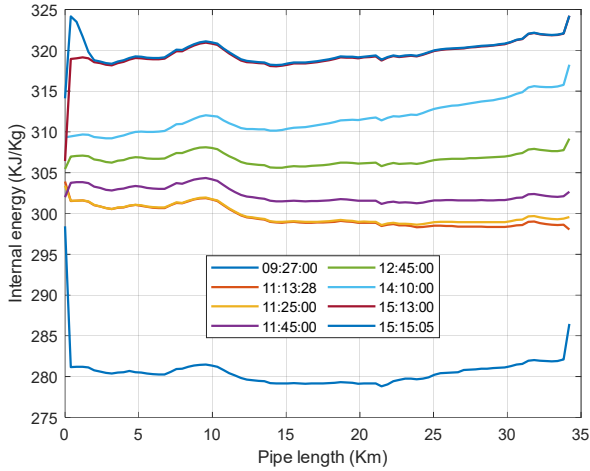


Figure 57- Distance plot of internal energy for different times during the kink-like-behavior of 8 June 2022.

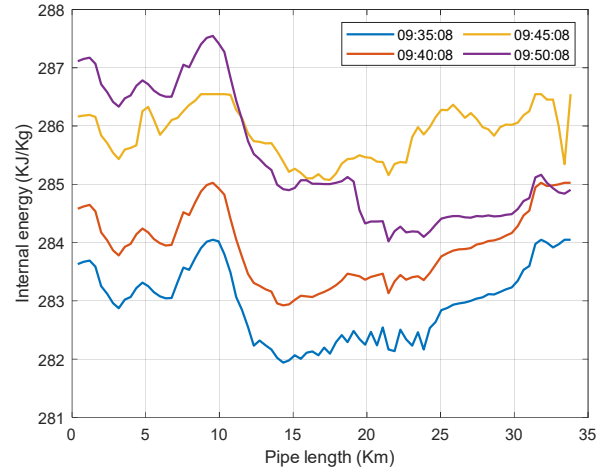


Figure 60- Internal energy for internal nodes on June 8, 2022.

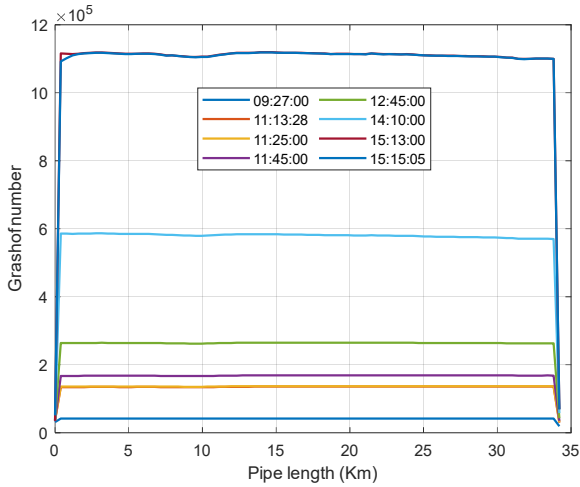


Figure 58- Distance plot of Grashof number for different times during the kink-like-behavior of 8 June 2022.

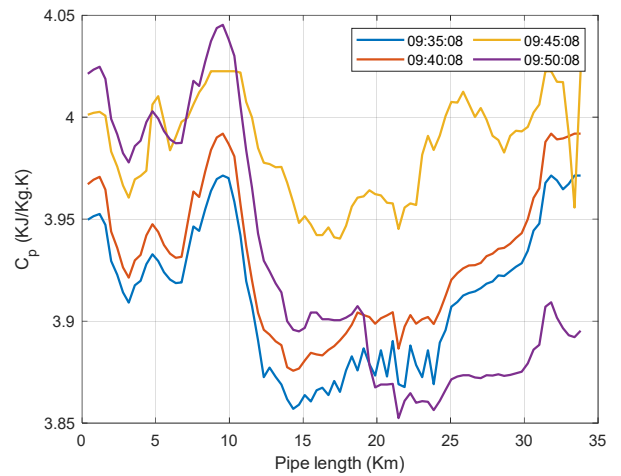


Figure 61- Specific heat capacity for constant pressure (c_p) for internal nodes on June 8, 2022.

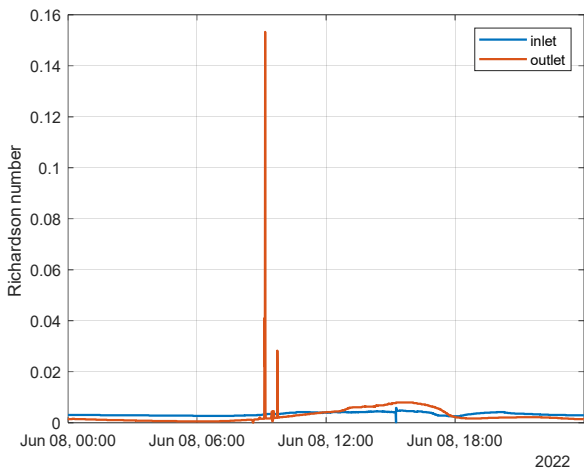


Figure 59- Richardson number at the inlet and outlet of the pipe on 8 June 2022.

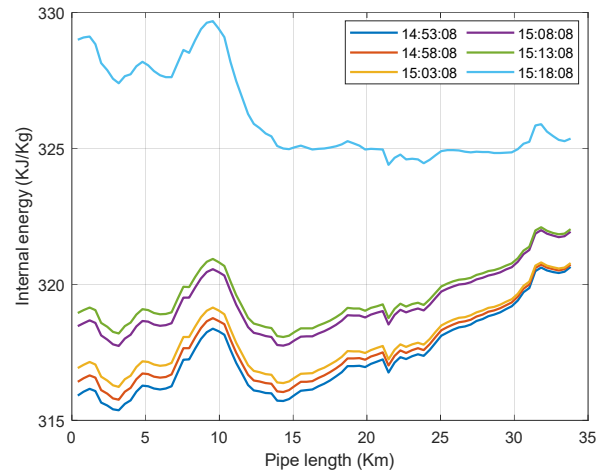


Figure 62- Internal energy for internal nodes on June 8, 2022.

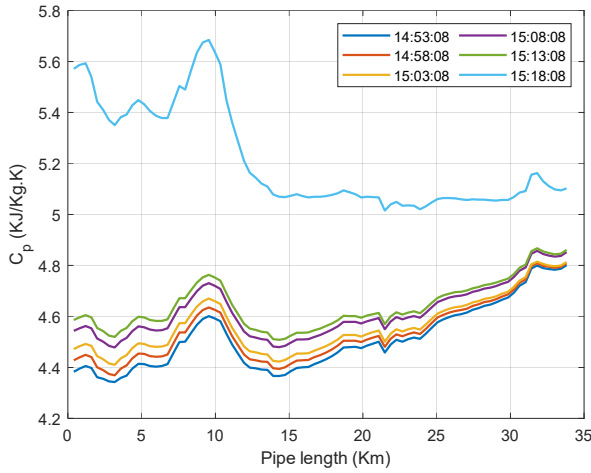


Figure 63- Specific heat capacity for constant pressure (C_p) for internal nodes on June 8, 2022.

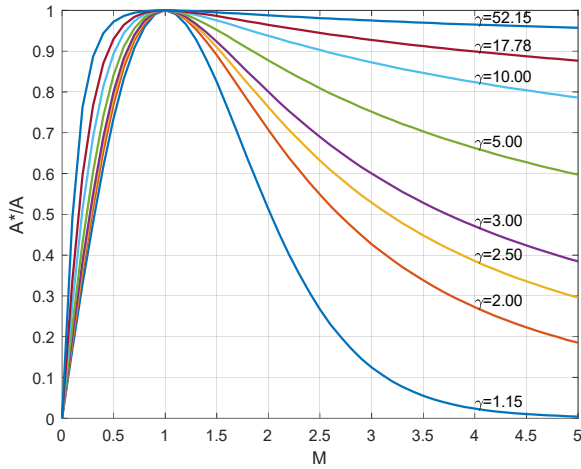


Figure 64- Hole Area over pipe area vs Mach number for different values of adiabatic heat index (Equation A1.14).

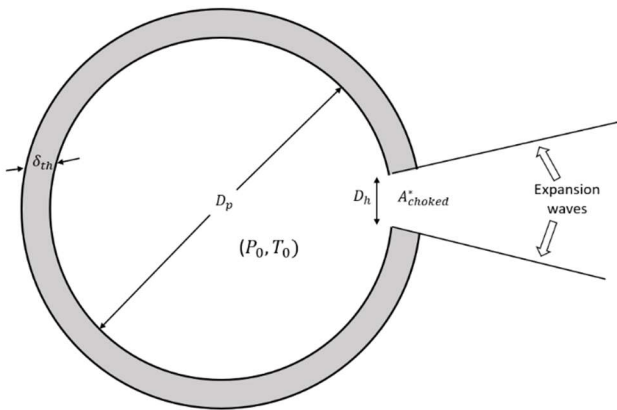


Figure 65-Schematic of the leakage from a hole on the pipe's wall.

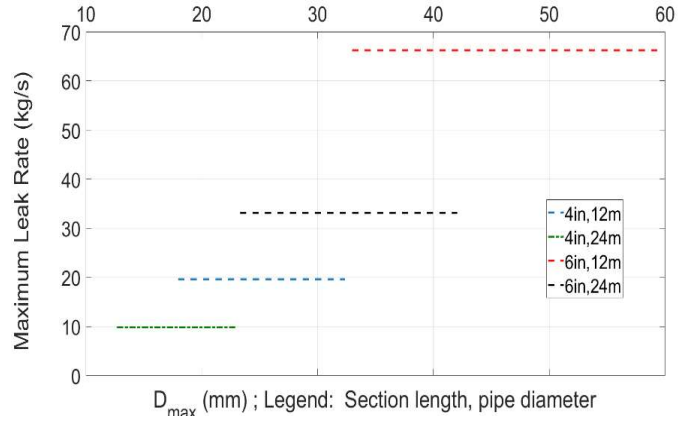


Figure 66-Maximum possible Rupture size (mm); different section length and pipe diameters (Legend) and heat ratios (start to end of each horizontal line).

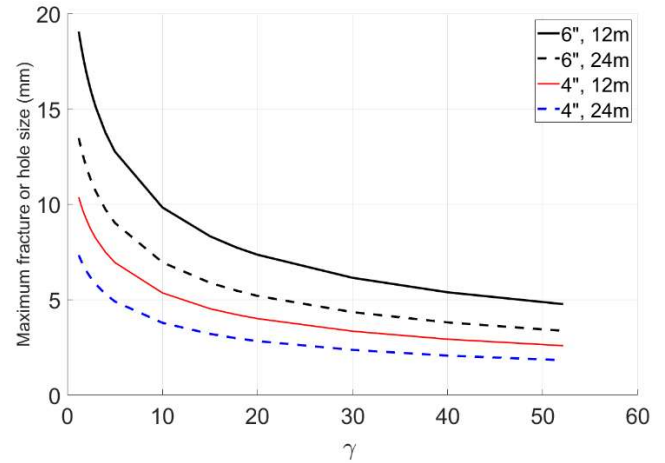


Figure 67-Maximum fracture or hole size (mm) versus adiabatic heat index γ tolerable before yielding and disintegration of the welded section.

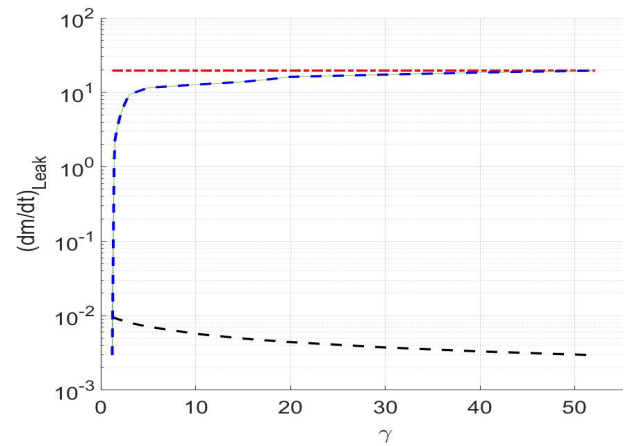


Figure 68-Leak Rate from Sensitivity threshold (bottom part of the plot in black) to the onset of yield stress of the pipeline (top part of the plot in red); Blue line is the leak rate behavior.